

Solving multi-pole challenges in the GW100 benchmark enables precise low-scaling GW calculations

Mia Schambeck,¹ Dorothea Golze,² and Jan Wilhelm^{1,*}

¹*Institute of Theoretical Physics and Regensburg Center for Ultrafast Nanoscopy (RUN),
University of Regensburg, 93053 Regensburg, Germany*

²*Faculty for Chemistry and Food Chemistry, Technische Universität Dresden, 01062 Dresden, Germany*
(Dated: August 26, 2024)

The GW approximation is a widely used method for computing electron addition and removal energies of molecules and solids. The computational effort of conventional GW algorithms increases as $O(N^4)$ with the system size N , hindering the application of GW to large and complex systems. Low-scaling GW algorithms are currently very actively developed. Benchmark studies at the single-shot G_0W_0 level indicate excellent numerical precision for frontier quasiparticle energies, with mean absolute deviations < 10 meV between low-scaling and standard implementations for the widely used GW100 test set. A notable challenge for low-scaling GW algorithms remains in achieving high precision for five molecules within the GW100 test set, namely O_3 , BeO, MgO, BN, and CuCN, for which the deviations are in the range of several hundred meV at the G_0W_0 level. This is due to a spurious transfer of spectral weight from the quasiparticle to the satellite spectrum in G_0W_0 calculations, resulting in multi-pole features in the self-energy and spectral function, which low-scaling algorithms fail to describe. We show in this work that including eigenvalue self-consistency in the Green's function (evGW₀) achieves a proper separation between satellite and quasiparticle peak, leading to a single solution of the quasiparticle equation with spectral weight close to one. evGW₀ quasiparticle energies from low-scaling GW closely align with reference calculations; the mean absolute error is only 12 meV for the five molecules. We thus demonstrate that low-scaling GW with self-consistency in G is well-suited for computing frontier quasiparticle energies.

I. INTRODUCTION

GW calculations [1–3] have become a standard tool for calculating electron addition and removal energies of molecules [4–6], two-dimensional materials [7–19] and solids [20–26]. Recent advancements of the GW method span a broad spectrum, including the application to deep core excitations [27–35], relativistic GW schemes [36–42], exploring excited-state potential energy surfaces from GW+Bethe-Salpeter [43–46], electron dynamics from Green's functions [47–58], and applying the GW methodology in magnetic fields [59–62]. There has also been a concerted effort towards benchmarking the accuracy of the GW method [63–66] and the numerical precision of GW implementations [5, 67–72]. An increasing number of machine learning models have emerged for predicting quasiparticle (QP) energies without performing a costly GW calculation [73–79]. Concerning method development beyond the GW approximation, vertex corrections [80–93] and connections with coupled-cluster methods [94–96] have been explored. Promising developments for the study of electronic excitations in the solid state have been also reported using coupled-cluster methods [97–103] and low-scaling Bethe-Salpeter approaches [104–106].

Despite that GW method development is blooming, several algorithmic bottlenecks render GW calculations challenging, particularly in dealing with complex or disordered systems with large simulation cells. In conventional GW implementations, the computational cost increases as $O(N^4)$ with the system size N , restricting conventional GW calculations often to systems with a few hundred atoms [2, 73]. Various strategies

have been devised to tackle this limitation, ranging from massively parallel implementations [107–113], to physically motivated approximations like embedding [114–119] and low-scaling techniques [120–136]. In this work, we focus on deterministic, low-scaling GW algorithms based on the GW space-time method by Rojas, Godby and Needs published in 1995 [120]. The GW space-time method relies on space-local representations and imaginary time-frequency transforms and achieves cubic scaling of the computational cost in the system size, $O(N^3)$, instead of quartic scaling $O(N^4)$ of conventional GW algorithms. Many different techniques have been used to increase the computational efficiency of the GW space-time method, including pair-atomic resolution of the identity [130, 137–140], separable density fitting [129, 135, 141–145], and global resolution of the identity with a local metric [14, 128, 134, 146, 147].

All of the space-time GW algorithms include three Fourier transforms between imaginary time and imaginary frequency, and vice versa, which are performed numerically. This poses a significant challenge in terms of numerical precision, a challenge that has been addressed by the development of tailored imaginary-time and imaginary-frequency grids [124, 148–150]. The precision of these numerical grids has undergone rigorous benchmarking against highly accurate GW calculations across various systems, including solids [124, 149], two-dimensional materials [149], and molecules [71, 134, 149]. Overall, the findings indicate excellent numerical precision, typically better than 10 meV for QP energies of the highest valence states and the lowest empty states [134, 149].

A notable challenge remains in achieving high precision for five molecules within the GW100 test set [5], namely O_3 , BeO, MgO, BN, and CuCN [134], at the single-shot G_0W_0 level of theory [2] using the Perdew-Burke-Ernzerhof (PBE) functional [151] for the underlying Kohn-Sham den-

* jan.wilhelm@physik.uni-regensburg.de

sity functional theory [152] (KS-DFT) calculation. We refer to this procedure as G_0W_0 @PBE. For these molecules, the G_0W_0 @PBE energies computed from low-scaling algorithms can differ by several hundred meV from reference calculations [134]. In this work, we revisit these five molecules and we aim to demonstrate that the multiple G_0W_0 @PBE solutions of the QP equation are unphysical and that a physically sound, single solution can be obtained using partial eigenvalue self-consistency in the Green's function or using a hybrid functional as starting point for G_0W_0 . We also aim to show that the low-scaling GW algorithms are numerically precise for the GW flavors which yield a single solution.

The article is organized as follows: We discuss the G_0W_0 scheme and multi-pole artifacts in the $GW100$ benchmark in Sec. II. We describe the low-scaling space-time GW algorithm in Sec. IV and the reference GW algorithm based on contour deformation in Sec. V. Computational details of our GW calculations are given in Sec. VI. We present and discuss G_0W_0 @PBE, $evGW_0$ and G_0W_0 @PBE0 calculations in Sec. VII, VIII and IX, respectively.

II. MULTISOLUTION ARTIFACTS AT THE G_0W_0 LEVEL

In this section, we briefly introduce the G_0W_0 approach and different methods to obtain the QP solution, including the evaluation of the spectral function. We showcase the issue of multisolution artifacts for the MgO gas phase molecule, which is part of the $GW100$ benchmark set [5].

The $GW100$ set is the standard molecular test set for assessing the accuracy of GW approaches and GW implementations [31, 67, 70, 71, 89, 128, 134, 143, 153–158]. $GW100$ contains one hundred small molecules with covalent and ionic bonds covering a wide range of the periodic table. The original $GW100$ study [5] reports the G_0W_0 @PBE QP energies of the highest occupied molecular orbital (HOMO) and the lowest occupied molecular orbital (LUMO) for all one hundred molecules. Those G_0W_0 @PBE data are the ones against which new low-scaling algorithms are typically benchmarked [71, 134, 149].

A G_0W_0 calculation starts from a self-consistent KS-DFT calculation [152],

$$[h_0(\mathbf{r}) + v_{xc}(\mathbf{r})]\psi_n(\mathbf{r}) = \varepsilon_n^{\text{DFT}}\psi_n(\mathbf{r}). \quad (1)$$

h_0 contains the kinetic energy, the Hartree potential and the external potential, while the exchange-correlation potential v_{xc} contains all electron-electron interactions beyond Hartree. $\psi_n(\mathbf{r})$ is the KS orbital n and $\varepsilon_n^{\text{DFT}}$ the associated KS eigenvalue. The terms G_0 and W_0 indicate that the Green's function G and the screened Coulomb interaction W are both computed using KS orbitals and KS eigenvalues, i.e., self-consistent updates of G and W from Green's function theory are omitted in G_0W_0 .

A central object in a G_0W_0 calculation is the G_0W_0 correlation self-energy which can be expressed as [2, 159]

$$\Sigma_n^c(\omega) = \sum_m \sum_s \frac{\langle \psi_n \psi_m | P_s | \psi_m \psi_n \rangle}{\omega - \varepsilon_m^{\text{DFT}} + (\Omega_s^{\text{RPA}} - i\eta) \text{sgn}(\varepsilon_F - \varepsilon_m^{\text{DFT}})}. \quad (2)$$

Here, ω denotes a frequency, ε_F the Fermi level of KS-DFT and $\eta > 0$ a broadening. Ω_s^{RPA} with $\Omega_1^{\text{RPA}} \leq \Omega_2^{\text{RPA}} \leq \dots$ are the charge-neutral singlet excitation energies computed using the random phase approximation (RPA), i.e. a vanishing exchange-correlation kernel [160] (see also discussion in Appendix B); P_s represents the product of transition densities of the excitation s . [2, 159]

One observable computed in a G_0W_0 calculation is the molecular spectral function, which takes the form of a many-body density of states [2, 161],

$$A(\omega) = \frac{1}{\pi} \text{Im } G(\omega) \text{sgn}(\varepsilon_F - \omega), \quad (3)$$

where $G(\omega)$ is the trace over spatial arguments of the single-particle Green's function. We express the spectral function as

$$A(\omega) = \sum_n A_n(\omega), \quad (4)$$

where n runs over all KS orbitals with a contribution $A_n(\omega)$ to the spectral function [2, 28, 124, 162]

$$A_n(\omega) = \frac{1}{\pi} \text{Im} \frac{\text{sgn}(\omega - \varepsilon_F)}{\omega - (\varepsilon_n^{\text{DFT}} + \Sigma_n^c(\omega) + i\eta + \Sigma_n^x - v_n^{\text{xc}})} \quad (5)$$

$$= \frac{1}{\pi} \frac{|\gamma|}{(\omega - (\varepsilon_n^{\text{DFT}} + \text{Re} \Sigma_n^c(\omega) + \Sigma_n^x - v_n^{\text{xc}}))^2 + \gamma^2}. \quad (6)$$

Here, $\gamma = \text{Im} \Sigma_n^c(\omega) + \eta$, $\Sigma^x(\mathbf{r}, \mathbf{r}')$ is the exchange self-energy [2] and Σ_n^x and v_n^{xc} are the n, n -diagonal elements of the respective quantities.

The peak positions $\varepsilon_n^{G_0W_0}$ of $A(\omega)$, known as QP energies, correspond to the negative of the ionization energies and to electron affinities of the molecule. QP energies are the frequencies where the real part of the denominator in Eq. (5) equals zero, i.e., the QP energies $\varepsilon_n^{G_0W_0}$ satisfy the QP equation

$$\varepsilon_n^{G_0W_0} = \varepsilon_n^{\text{DFT}} + \text{Re} \Sigma_n^c(\varepsilon_n^{G_0W_0}) + \Sigma_n^x - v_n^{\text{xc}}. \quad (7)$$

The non-linearity of $\Sigma_n^c(\omega)$ with respect to ω , allows for multiple solutions $\varepsilon_n^{G_0W_0}$ for a given level n . Such multiple solutions have been observed for five molecules in the $GW100$ test, namely O_3 , BeO , MgO , BN , and CuCN at the G_0W_0 @PBE level [5].

We illustrate multiple solutions of Eq. (7) for state $n = \text{HOMO}$ of the MgO molecule, see Fig. 1(a). The black dashed traces visualize the linear function

$$f(\omega) = \omega - (\varepsilon_{\text{HOMO}}^{\text{DFT}} + \Sigma_{\text{HOMO}}^x - v_{\text{HOMO}}^{\text{xc}}) \quad (8)$$

such that the intersections ε of $f(\omega)$ and $\text{Re} \Sigma_{\text{HOMO}}^c(\omega)$, $f(\varepsilon) = \text{Re} \Sigma_{\text{HOMO}}^c(\varepsilon)$, are the solutions of the QP equation (7). Five intersections are apparent, $\varepsilon \in \{-11.00 \text{ eV}, -9.90 \text{ eV}, -7.09 \text{ eV}, -6.91 \text{ eV}, -6.68 \text{ eV}\}$, where the highest solution has been picked in the original work [5] as G_0W_0 @PBE HOMO energy. The large number of intersections is due to the many poles in the self-energy (2).

Each intersection ε comes with a spectral weight Z_ε that quantifies the number of electrons associated with a given

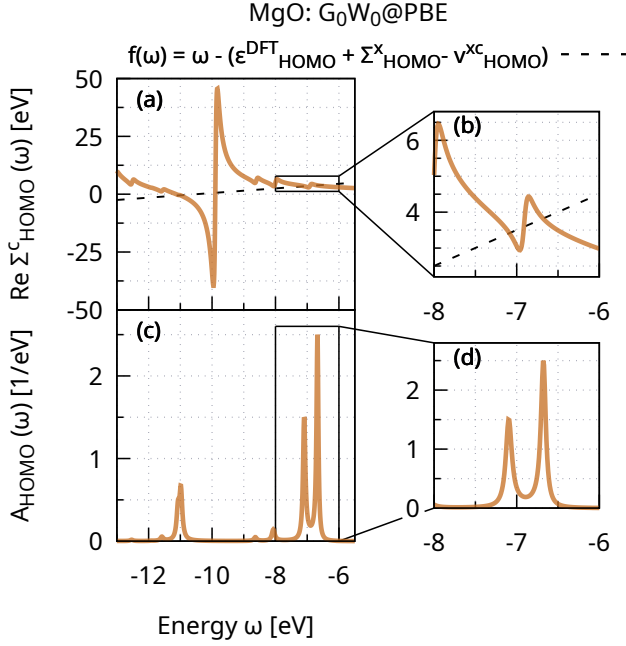


FIG. 1. (a)/(b) Real part of the G_0W_0 @PBE HOMO self-energy $\Sigma_{\text{HOMO}}^c(\omega)$, Eq. (2), for the MgO molecule from the GW100 set. Intersections of the straight line $f(\omega)$ and $\text{Re}\Sigma_{\text{HOMO}}^c(\omega)$ lead to five solutions of the QP equation (7), as already discussed in Ref. 5. (c)/(d) G_0W_0 @PBE HOMO contribution $A_{\text{HOMO}}(\omega)$ to the spectral function, Eq. (5). We have computed all quantities using the numerically precise contour deformation as implemented in FHI-aims [27] and a broadening $\eta = 1$ mHa, see further details in Sec. V and VI.

peak in the spectral function. Z_ε is usually approximately computed as

$$Z_\varepsilon \approx \left[1 - \text{Re} \frac{\partial \Sigma_n^c(\omega)}{\partial \omega} \bigg|_{\omega=\varepsilon} \right]^{-1}, \quad (9)$$

see Appendix A for a derivation. Due to the small slope of $\Sigma_{\text{HOMO}}^c(\omega)$ at the intersections $\varepsilon \in \{-7.09 \text{ eV}, -6.68 \text{ eV}\}$, the associated spectral weight is large, whereas the other intersections exhibit a relatively small spectral weight. This is also apparent in the HOMO contribution $A_{\text{HOMO}}(\omega)$ to the G_0W_0 @PBE spectral function (5), see Fig. 1(c)/(d). Three major peaks are visible at -11.0 eV , -7.09 eV and -6.68 eV , precisely located at intersections of $f(\omega)$ and $\text{Re}\Sigma_{\text{HOMO}}^c(\omega)$. In particular, the two peaks at $\varepsilon \in \{-7.09 \text{ eV}, -6.68 \text{ eV}\}$ carry both significant spectral weight, i.e. a distinct single QP peak is absent.

A closer inspection of $\Sigma_{\text{HOMO}}^c(\omega)$ at the two intersections $\varepsilon \in \{-7.09 \text{ eV}, -6.68 \text{ eV}\}$ in Fig. 1(b) reveals a shallow pole of $\text{Re}\Sigma_{\text{HOMO}}^c(\omega)$ at $\omega_{\text{pole}}^{\text{MgO}} = -6.91 \text{ eV}$. As evident from Eq. (2), poles in the real part of the self-energy occur at

$$\omega_{\text{pole}} = \varepsilon_i^{\text{DFT}} - \Omega_s^{\text{RPA}} \quad \text{or} \quad \omega_{\text{pole}} = \varepsilon_a^{\text{DFT}} + \Omega_s^{\text{RPA}}, \quad (10)$$

where i denotes an occupied and a an empty KS orbital index. For a calculation with $2N_{\text{el}}$ electrons and N_{basis} basis functions, this makes in total $N_s = N_{\text{el}}(N_{\text{basis}} - N_{\text{el}})$ excitation energies $\Omega_s^{\text{RPA}}, s = 1, \dots, N_s$ and thus $N_{\text{basis}}N_s$ poles in

TABLE I. PBE and PBE0 eigenvalues and excitation energies $\Omega_s^{\text{TDDFT/RPA}}$ from time-dependent DFT (TDDFT) and RPA of the MgO molecule. All values in eV. In Appendix B, we give details on TDDFT and RPA and we discuss the origin of the relationship $\Omega_1^{\text{PBE}} \approx \Omega_1^{\text{PBE0}} \approx \Omega_1^{\text{RPA@PBE}} \ll \Omega_1^{\text{RPA@PBE0}}$. TDDFT and RPA excitation energies have been computed using pyscf [163].

	PBE	PBE0
$\varepsilon_{\text{HOMO}-3}^{\text{DFT}}$	-19.52	-22.13
$\varepsilon_{\text{HOMO}-2}^{\text{DFT}}$	-6.09	-6.87
$\varepsilon_{\text{HOMO}}^{\text{DFT}} = \varepsilon_{\text{HOMO}-1}^{\text{DFT}}$	-4.79	-6.07
$\varepsilon_{\text{LUMO}}^{\text{DFT}}$	-4.29	-3.60
$\Omega_{s=1}^{\text{TDDFT}} = \Omega_{s=2}^{\text{TDDFT}}$	0.67	0.62
$\Omega_{s=1}^{\text{RPA}} = \Omega_{s=2}^{\text{RPA}}$	0.82	2.83
$\Omega_{s=3}^{\text{TDDFT}}$	2.87	2.86
$\Omega_{s=3}^{\text{RPA}}$	3.21	4.91

$\Sigma_{\text{HOMO}}^c(\omega)$ [164]. We list KS eigenvalues and RPA charge-neutral excitation energies Ω_s^{RPA} of MgO in Table I and we identify the self-energy pole at -6.91 eV based on Table I as

$$\omega_{\text{pole}}^{\text{MgO}} = \varepsilon_{\text{HOMO}-2}^{\text{PBE}} - \Omega_{s=1}^{\text{RPA@PBE}} = -6.91 \text{ eV}. \quad (11)$$

Poles in the real-part of the self-energy have corresponding peaks in the imaginary part of Σ^c [2]. A distinct QP peak in $A_n(\omega)$ at $\omega = \varepsilon^*$ emerges when $\text{Im}\Sigma^c$ is small, as obvious from Eq. (6). This is the case when the QP peak is far away from any pole of $\text{Re}\Sigma_{\text{HOMO}}^c(\omega)$. The spectral weight Z_{ε^*} of the QP peak is then close to one because of a small slope of the self-energy, $|\text{Re}\partial_\omega \Sigma_n^c(\omega = \varepsilon^*)| \ll 1$ [2]. Further intersections of $f(\omega)$ and $\text{Re}\Sigma_{\text{HOMO}}^c(\omega)$ exist at energies lower than $\omega = \varepsilon^*$. All these solutions are close to a pole in $\text{Re}\Sigma_{\text{HOMO}}^c(\omega)$. $\text{Im}\Sigma^c$ is consequently large, resulting in low spectral weights. In other words, we obtain further solutions with satellite character. In the molecular case, satellites are due to multielectron excitations, i.e., the charged electron or hole excitation couples to charge-neutral electronic excitations.

The PBE eigenvalues $\varepsilon_i^{\text{PBE}}$ of occupied KS states are overestimated and usually a few electron volts higher in energy compared to the GW energies. The poles at $\varepsilon_i^{\text{PBE}} - \Omega_s^{\text{RPA}}$ are therefore at too high frequencies. Or in other words, the satellites occur erroneously at too high energy and are too close to the QP peak. For HOMO excitations computed at the G_0W_0 @PBE level, satellites and QP peak are still well separated for most molecules and solids. Exceptions are, for example, the five molecules we discuss in this work. As we demonstrated for MgO, $\omega_{\text{pole}}^{\text{MgO}} = \varepsilon_{\text{HOMO}-2}^{\text{PBE}} - \Omega_{s=1}^{\text{RPA}}$ is located close to the QP solution. This results in an erroneous redistribution of spectral weight from the QP to the satellite solution, ultimately causing the observed multisolution behavior. The location of the satellites becomes increasingly incorrect for deeper excitations. While $\varepsilon_i^{\text{PBE}}$ is overestimated by a few electron volts for HOMO excitations, this overestimation is significantly larger, around 20–30 eV for 1s excitations

of second-row elements [27]. In these cases, the poles are drastically too high in energy and the satellites always overlap with the QP solution, leading to a pronounced multisolution scenario with no identifiable QP peak at the G_0W_0 @PBE level [28, 33]. This stands in stark contrast to experimental observations, where one sharp 1s main peak with very small satellites is observed in X-ray photoemission spectra of closed shell molecules [165–167].

We observe similar multi-solution behaviour as described for MgO for the HOMO of BeO, BN, O₃ and CuCN from the GW100 set, see Fig. 5 and 6 in the appendix. These multiple solutions at the G_0W_0 @PBE level are not only unphysical as discussed above, but they also pose a numerical challenge to low-scaling GW algorithms [128, 134]. In this work, we address this issue.

III. CORRECTION OF MULTIPOLE ARTIFACTS WITH EIGENVALUE-SELFCONSISTENCY IN G

The crucial role of eigenvalue self-consistency in the Green's function (evG) has long been recognized in the literature [33, 75, 164, 168–171] as essential for preventing an artificial transfer of spectral weight from the QP peak to the satellites and suppressing multisolution behavior. We denote this procedure as evGW₀ where W is fixed at the G_0W_0 level, while G in Eq. (23) is recomputed from Eq. (16) using the QP energies (7). This procedure is repeated until self-consistency in the QP energies ϵ_m^{QP} is reached [2]. In evGW₀, the energies ϵ_m^{DFT} in Eq. (2) are replaced by $\epsilon_m^{\text{QP}} = \epsilon_m^{\text{DFT}} + \Delta_m^{\text{QP}}$, where Δ_m^{QP} is the QP correction for state m . The poles of $\text{Re } \Sigma_n^c(\omega)$ (Eq. (2)) in evGW₀ are consequently at

$$\omega_{\text{pole}} = \epsilon_i^{\text{DFT}} + \Delta_i^{\text{QP}} - \Omega_s^{\text{RPA}} \quad \text{for occupied orbital } i, \quad (12)$$

$$\omega_{\text{pole}} = \epsilon_a^{\text{DFT}} + \Delta_a^{\text{QP}} + \Omega_s^{\text{RPA}} \quad \text{for empty orbital } a. \quad (13)$$

When using the PBE functional in KS-DFT, Δ_m^{QP} is usually negative for occupied states and positive for the empty states. Compared to G_0W_0 @PBE, poles at frequency below the Fermi level thus often shift to more negative frequencies and poles at frequencies above the Fermi level to more positive frequencies. We will demonstrate this for the MgO case in Section VIII.

We want to assess now in which frequency ranges poles in $\text{Re } \Sigma_n^c(\omega)$ occur at the evGW₀ level, following the discussion of V  ril *et al.* [164]. In addition to requiring evG, we also assume positive, non-zero singlet RPA excitation energies $\Omega_s^{\text{RPA}} > 0$, which should be the case for weakly correlated systems. For every level n close to HOMO and LUMO with

$$\epsilon_n^{\text{QP}} \in [\epsilon_{\text{HOMO}}^{\text{QP}} - \Omega_1^{\text{RPA}}, \epsilon_{\text{LUMO}}^{\text{QP}} + \Omega_1^{\text{RPA}}], \quad (14)$$

the denominator of $\Sigma_n^c(\omega)$ in Eq. (2) is strictly non-zero (even for $\eta \rightarrow 0$) because Eq. (14) implies

$$\omega - \epsilon_i^{\text{QP}} + \Omega_s^{\text{RPA}} > 0 \quad \text{for } \omega = \epsilon_n^{\text{QP}}, \text{ occupied orbital } i, \text{ all } s,$$

$$\omega - \epsilon_a^{\text{QP}} - \Omega_s^{\text{RPA}} < 0 \quad \text{for } \omega = \epsilon_n^{\text{QP}}, \text{ empty orbital } a, \text{ all } s.$$

Therefore, $\Sigma_n^c(\omega = \epsilon_n^{\text{QP}})$ is never singular for evG, $\Omega_s > 0$, and n with (14) [164]. Poles of $\text{Re } \Sigma_n^c(\omega)$ only appear at energies

$$\omega_{\text{pole}}^{\text{evGW}_0} \in [-\infty, \epsilon_{\text{HOMO}}^{\text{QP}} - \Omega_1^{\text{RPA}}] \cup [\epsilon_{\text{LUMO}}^{\text{QP}} + \Omega_1^{\text{RPA}}, \infty]. \quad (15)$$

When considering $n = \text{HOMO}$ or $n = \text{LUMO}$ in evG with $\Omega_s^{\text{RPA}} > 0$, all poles $\omega_{\text{pole}}^{\text{evGW}_0}$ of $\Sigma_{\text{HOMO/LUMO}}^c(\omega)$ are thus separated from $\omega = \epsilon_{\text{HOMO/LUMO}}^{\text{QP}}$ by the energy Ω_1^{RPA} . By design, multiple solutions will not occur at the evGW₀ level for HOMO and LUMO, given that the system has a non-zero optical gap. Furthermore, it has also been shown that evGW₀ suppresses multisolution behavior for deeper states, inhibiting erroneous transfer of spectral weights from QP peak to satellites [28, 170]. We note that Eqs. (12)–(15) hold also for the evGW scheme, where eigenvalues are also iterated in W .

A computationally less expensive alternative to evG is introducing the so-called Hedin shift [1, 2, 75, 168, 171, 172] in the denominator of Eq. (2). The Hedin shift can be viewed as an approximation to evGW₀, where the individual shifts Δ_m^{QP} in Eqs. (12) and (13) are approximated with a global shift ΔH . Another alternative is to start the G_0W_0 calculation from a hybrid DFT starting point, such as PBE0. In G_0W_0 @PBE0, the poles will effectively also shift to more negative frequencies below the Fermi level because $\epsilon_i^{\text{PBE0}} < \epsilon_i^{\text{PBE}}$ and $\Omega_s^{\text{RPA@PBE0}} > \Omega_s^{\text{RPA@PBE}}$, as shown in Table I. We note that the latter was also discussed in literature before [28, 70].

In this work, we aim to show that low-scaling GW is numerically precise for computing frontier QP energies from GW schemes that are free of multipole artifacts.

IV. LOW-SCALING GW SPACE-TIME ALGORITHM

Many low-scaling GW algorithms [122–124, 127–132, 134, 143] build on the GW space-time method [120]. In this work, we execute GW calculations using the low-scaling algorithm from Ref. 134 which adapts the space-time method for use with Gaussian basis functions. In order to introduce the basic idea of the GW space-time method, we use a generic formulation in this section for non-periodic systems projecting all quantities on real-space grids. It is important to note that this formulation differs from the original GW space-time method [120] where some quantities were calculated using a plane-wave basis set.

KS orbitals and eigenvalues are used to calculate the single-particle Green's function in imaginary time,

$$G(\mathbf{r}, \mathbf{r}', i\tau) = \begin{cases} i \sum_i^{\text{occ}} \psi_i(\mathbf{r}) \psi_i^*(\mathbf{r}') e^{-|(\epsilon_i^{\text{DFT}} - \epsilon_F)\tau|}, & \tau < 0, \\ -i \sum_a^{\text{virt}} \psi_a^*(\mathbf{r}) \psi_a(\mathbf{r}') e^{-|(\epsilon_a^{\text{DFT}} - \epsilon_F)\tau|}, & \tau > 0, \end{cases} \quad (16)$$

where the sum over the index i runs over all occupied KS orbitals and the sum over the index a over all virtual, i.e., empty KS orbitals. ϵ_F is the Fermi level. We note that for the non-relativistic molecular calculations conducted in this work, the

KS orbitals are real-valued. The irreducible polarizability follows,

$$\chi^0(\mathbf{r}, \mathbf{r}', i\tau) = -iG(\mathbf{r}, \mathbf{r}', i\tau)G(\mathbf{r}, \mathbf{r}', -i\tau), \quad (17)$$

which is then transformed to imaginary frequency,

$$\chi^0(\mathbf{r}, \mathbf{r}', i\omega) = i \int_{-\infty}^{\infty} e^{-i\omega\tau} \chi^0(\mathbf{r}, \mathbf{r}', i\tau) d\tau. \quad (18)$$

This transform can be understood as Laplace transform followed by analytic continuation to the imaginary axis and effectively takes the form of a Fourier transform [121]. Next, the dielectric function ε can be calculated in imaginary frequency from the irreducible polarizability,

$$\varepsilon(\mathbf{r}, \mathbf{r}', i\omega) = \delta(\mathbf{r}, \mathbf{r}') - \int d\mathbf{r}'' v(\mathbf{r}, \mathbf{r}'') \chi^0(\mathbf{r}'', \mathbf{r}', i\omega), \quad (19)$$

using the Dirac delta function $\delta(\mathbf{r}, \mathbf{r}')$ and the Coulomb interaction $v(\mathbf{r}, \mathbf{r}') = 1/|\mathbf{r} - \mathbf{r}'|$. The screened Coulomb interaction can be computed from the inverse dielectric function,

$$W(\mathbf{r}, \mathbf{r}', i\omega) = \int d\mathbf{r}'' \varepsilon^{-1}(\mathbf{r}, \mathbf{r}'', i\omega) v(\mathbf{r}'', \mathbf{r}'). \quad (20)$$

It is convenient in GW implementations to split the screened interaction W into the bare Coulomb interaction v and the correlation part W^c ,

$$W^c(\mathbf{r}, \mathbf{r}', i\omega) = W(\mathbf{r}, \mathbf{r}', i\omega) - v(\mathbf{r}, \mathbf{r}'). \quad (21)$$

In the space-time method, W^c is required in imaginary time,

$$W^c(\mathbf{r}, \mathbf{r}', i\tau) = \frac{i}{2\pi} \int_{-\infty}^{\infty} e^{i\omega\tau} W^c(\mathbf{r}, \mathbf{r}', i\omega) d\omega, \quad (22)$$

and the correlation self-energy is given as product of the Green's function and the screened Coulomb interaction,

$$\Sigma^c(\mathbf{r}, \mathbf{r}', i\tau) = iG(\mathbf{r}, \mathbf{r}', i\tau)W^c(\mathbf{r}, \mathbf{r}', i\tau). \quad (23)$$

The self-energy is then transformed to imaginary frequency,

$$\Sigma^c(\mathbf{r}, \mathbf{r}', i\omega) = i \int_{-\infty}^{\infty} e^{-i\omega\tau} \Sigma^c(\mathbf{r}, \mathbf{r}', i\tau) d\tau, \quad (24)$$

and we calculate its (n, n) -diagonal element,

$$\begin{aligned} \Sigma_n^c(i\omega) &= \langle \psi_n | \Sigma^c(i\omega) | \psi_n \rangle \\ &= \int d\mathbf{r} d\mathbf{r}' \psi_n^*(\mathbf{r}) \Sigma^c(\mathbf{r}, \mathbf{r}', i\omega) \psi_n(\mathbf{r}'). \end{aligned} \quad (25)$$

The self-energy is then analytically continued to real frequency, i.e. we determine the fit parameters $a_{j,n}$ and $b_{j,n}$ of an N -parameter Padé approximant $P_n(i\omega)$ [5, 173] to match $\Sigma_n^c(i\omega)$ of QP level n as closely as possible,

$$\Sigma_n^c(i\omega) \approx P_n(i\omega) = \frac{\sum_{j=1}^{(N-1)/2} a_{j,n} \cdot (i\omega)^j}{1 + \sum_{j=1}^{N/2} b_{j,n} \cdot (i\omega)^j}. \quad (26)$$

Based on the identity theorem for analytic functions [174], one evaluates P_n at real frequencies to compute the self-energy at real frequencies, $\Sigma_n^c(\omega) \approx P_n(\omega)$ [2, 5].

Focusing on the G_0W_0 method already introduced before, we use KS orbitals to approximate the QP wavefunctions and we compute G and W only once using KS orbitals and KS eigenvalues from Eqs. (16)–(20). The QP energies $\varepsilon_n^{G_0W_0}$ can finally be calculated by solving the QP equation (7).

The computational cost of the presented algorithm increases with $O(N^3)$ in the system size N . This is apparent from Eq. (16), which requires $O(N_{\text{grid}}^2(N_{\text{occ}} + N_{\text{vir}})) = O(N^3)$ number of floating point operations, where N_{grid} is the number of real-space grid points, N_{occ} the number of occupied KS orbitals, and N_{vir} the number of virtual KS orbitals.

In a standard GW algorithm, a computational bottleneck is evaluating the Adler-Wiser formula [175, 176] for the irreducible polarizability in imaginary frequency,

$$\chi^0(\mathbf{r}, \mathbf{r}', i\omega) = \sum_i^{\text{occ}} \sum_a^{\text{virt}} \frac{2(\varepsilon_i - \varepsilon_a)}{(\varepsilon_i - \varepsilon_a)^2 + \omega^2} \psi_i(\mathbf{r}) \psi_a^*(\mathbf{r}) \psi_i^*(\mathbf{r}') \psi_a(\mathbf{r}'). \quad (27)$$

This computation requires $O(N_{\text{grid}}^2 N_{\text{occ}} N_{\text{virt}}) = O(N^4)$ operations, and is thus computationally more demanding than the whole low-scaling algorithm (16)–(24) for a large system.

The drawback of algorithm (16)–(24) is that it requires very fine real-space grids, in particular when evaluating Coulomb interactions in Eq. (19) and (20). This is why the original GW space-time method [120] used a plane-waves basis for the calculation of $\varepsilon(i\omega)$ and $W(i\omega)$. Then, the $O(N^3)$ -scaling convolutions (19) and (20) in real space transform into $O(N^2)$ multiplications in the plane-wave basis. The inversion of $\varepsilon(i\omega)$ remains as cubic-scaling step. For the low-scaling GW implementation used in this work [134], Eq. (16)–(24) have been reformulated in a Gaussian basis set resulting in effective $O(N^2)$ scaling [128, 134].

V. REFERENCE GW CALCULATIONS WITH CONTOUR DEFORMATION

In the low-scaling GW space-time method, one major challenge regarding numerical precision is the analytic continuation of $\Sigma^c(i\omega)$ to $\Sigma^c(\omega)$. A numerically more precise procedure for computing $\Sigma^c(\omega)$ is the contour deformation (CD) [2, 27, 177–179]. The starting point of CD is Eq. (23), formulated in real frequency, [2]

$$\Sigma^c(\mathbf{r}, \mathbf{r}', \omega) = \frac{i}{2\pi} \int_{-\infty}^{\infty} G(\mathbf{r}, \mathbf{r}', \omega + \omega') W^c(\mathbf{r}, \mathbf{r}', \omega') d\omega'. \quad (28)$$

Due to the pole structure of G and W on the real-frequency axis, the numerical integration of Eq. (28) is potentially unstable [2]. One way to circumvent this problem is to rewrite

Eq. (28) with a contour integral,

$$\begin{aligned} \Sigma^c(\mathbf{r}, \mathbf{r}', \omega) = & \frac{i}{2\pi} \oint d\omega' G(\mathbf{r}, \mathbf{r}', \omega + \omega') W^c(\mathbf{r}, \mathbf{r}', \omega') \\ & - \frac{1}{2\pi} \int_{-\infty}^{\infty} d\omega' G(\mathbf{r}, \mathbf{r}', \omega + i\omega') W^c(\mathbf{r}, \mathbf{r}', i\omega'), \end{aligned} \quad (29)$$

where the closed integral comprises the real axis, two arcs and the imaginary axis. The closed integral can be calculated using Cauchy's residue theorem, while the imaginary axis can be integrated numerically since the problematic pole structure of G and W is restricted to the real frequency axis. [2] QP energies from CD follow from solving the QP equation (7).

The scaling for evaluating the self-energy from CD is $O(N^4)$ for a single valence excitation [27], which is an order higher than the $O(N^3)$ -scaling of the GW space-time method. CD is numerically highly accurate. It was shown that CD reproduces the exact self-energy structure by comparing with fully analytic solutions obtained by evaluating Eq. (2) [27]. We use therefore the CD approach as reference to assess the numerical precision of our low-scaling GW algorithm. More details on CD can be found in Refs. 2 and 27.

VI. COMPUTATIONAL DETAILS

A. Low-scaling GW calculations using CP2K

The low-scaling GW space-time algorithm used in this work [134] is implemented in the CP2K software package [180, 181]. CP2K employs a Gaussian basis set for representing KS orbitals. We use the Gaussian and augmented plane-waves scheme (GAPW) [182] in CP2K which allows for all-electron calculations. The low-scaling G_0W_0 implementation [134] is a reformulation of the space-time method [120] in a Gaussian basis set, where sparsity is introduced by combining a global resolution-of-the-identity (RI) scheme with a truncated Coulomb metric [146, 147].

For expanding KS orbitals, we use the def2-QZVP basis set [183] with an RI-cc-pV5Z auxiliary basis [184]. We choose a minimax time-frequency grid [124, 148, 149, 185] with 30 points for all low-scaling GW calculations. For the RI with the truncated Coulomb metric we set a truncation radius of 3 Å [146, 147]. We compute two- and three-center integrals over Gaussians using recursive, analytical schemes [186, 187]. The self-energy is analytically continued from imaginary frequency to the real frequency using a Padé model [5, 173] with 16 parameters. We broaden the spectral functions using $\eta = 1$ mHa = 27.2 meV in Eq. (5).

B. Reference GW calculations with contour deformation using FHI-aims

We use the CD- GW algorithm [27] as implemented in the FHI-aims software package [188]. FHI-aims is an all-electron electronic structure code using numerical atom-centered orbitals (NAO) for expanding KS orbitals [188]. We use the

Gaussian def2-QZVP [183] basis set, which can be also represented as NAO basis, and an automatically generated RI basis set. In the CD, we employ a modified Gauss-Legendre grid [189] for the evaluation of the imaginary-frequency integral term, setting the number of frequency points to 2000 to obtain benchmark quality. The broadening parameter [27] is set to a rather large value $\eta = 4$ mHa = 108.8 meV to facilitate the convergence in the evG_0W_0 case. The only exception is that for Fig. 1, we use a smaller broadening of 1 mHa to obtain sharp and well-separated peaks in the spectral function. The broadening of peaks in the spectral function resulting from CD differs from that of analytic continuation, as outlined in Ref. 27. Therefore it is difficult to directly compare peak widths and heights in the spectral function between CD and analytic continuation.

VII. LOW-SCALING G_0W_0 @PBE CALCULATIONS ON O_3 , BeO, MgO, BN, CuCN

In this section we present low-scaling G_0W_0 @PBE calculations on the five molecules, O_3 , BeO, MgO, BN, and CuCN, and we will discuss the challenges that occurred.

It was already observed in the original $GW100$ work [5] that computing the G_0W_0 @PBE HOMO energy of O_3 , BeO, MgO, BN, and CuCN posed a significant numerical challenge. In the analytic continuation, this challenge was addressed by employing a 128-pole function to fit $\Sigma_{\text{HOMO}}^c(i\omega)$ for obtaining $\Sigma_{\text{HOMO}}^c(\omega)$ along the real-frequency axis. This high-precision fit was essential for accurately computing the G_0W_0 @PBE HOMO energy from the QP equation (7) for the five aforementioned molecules. For all other 95 molecules, a 16-pole fit on Σ_{HOMO}^c was sufficient for accurately computing the G_0W_0 @PBE HOMO energy.

GW space-time algorithms require in general three transforms between imaginary time and imaginary frequency, as discussed in Sec. IV. These transforms are executed numerically using discrete time and frequency grids. The functions in imaginary time and frequency usually have long tails and localized features. The usual Fast Fourier Transform with homogeneously spaced integration grids would need a large number of discrete time or frequency points. Instead, a non-equidistant Fourier transform can reduce the number of time and frequency points drastically [124, 149]. Non-equidistant grids can be set up through various techniques aimed at identifying discrete points that are optimal in a certain sense. Such approaches include the minimax approximation [124, 128, 134, 148, 149, 190–193] or least-square quadratures [130, 194–198]. Both algorithms have in common that they are numerically ill-conditioned and grid generation is typically restricted to less than 100 grid points. For instance, the recently introduced GreenX library [148] offers minimax time and frequency grids, each containing up to 34 points [148, 149, 199]. Consequently, when utilizing time and frequency grids from the GreenX library, the number of parameters available for fitting $\Sigma^c(i\omega)$ is limited to 34. This is not sufficient for accurately computing the G_0W_0 @PBE HOMO energy of the five challenging molecules, O_3 , BeO,

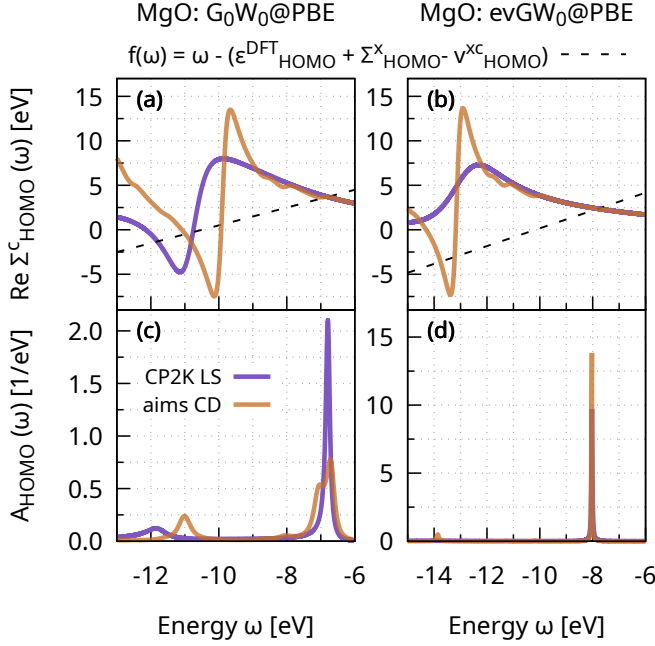


FIG. 2. Real part of the HOMO self-energy $\Sigma_{\text{HOMO}}^c(\omega)$ [G_0W_0 @PBE in (a) and $\text{ev}G_0W_0$ @PBE in (b)] and the HOMO contribution to the spectral function $A_{\text{HOMO}}(\omega)$ [Eq. (5), G_0W_0 @PBE in (c) and $\text{ev}G_0W_0$ @PBE in (d)] for the molecule MgO; computed from low-scaling GW in the CP2K package [134] ("CP2K LS"; violet traces) and from the highly accurate CD as implemented in FHI-aims [27] ("aims CD"; brown traces). $\text{Re}\Sigma_{\text{HOMO}}^c(\omega)$ and $A(\omega)$ for the other four numerically challenging molecules BeO, O_3 , BN, CuCN from the GW100 test set [5] are available in Figs. 6 and 7 for G_0W_0 @PBE and $\text{ev}G_0W_0$ @PBE in the appendix.

MgO, BN, CuCN, [128, 134, 149] which required a fit with a 128-pole model [5], that requires at least 128 imaginary-frequency points.

We now use our low-scaling GW implementation [134] to compute the G_0W_0 @PBE self-energy and spectral function. The results for the MgO molecule are shown as violet traces in Fig. 2(a) and (c). Low-scaling GW [134] fails to reproduce the shallow self-energy pole at $\omega_{\text{pole}} \approx -6.91$ eV [Fig. 2(a) and zoom in Fig. 1(b)] which results in a single peak of the spectral function at $\omega \approx -6.9$ eV [Fig. 2(c)] instead of the split peak present in the reference CD calculation [Fig. 2(c)]. The same failure in computing the self-energy has been observed in the original work, Ref. 5 (Fig. 13), when using analytical continuation with a 16-pole approximant to the self-energy. When using a 128-pole approximant for analytical continuation all poles of the self-energy were correctly reproduced [5]. The low-scaling GW implementation [134] is currently restricted to at most 34 imaginary-frequency points, and thus 34 fit parameters for analytic continuation. The Padé model is thus not flexible enough to accurately reproduce the G_0W_0 @PBE self-energy matrix elements for the HOMO of MgO. The same observation is made for O_3 , BeO, BN, and CuCN (Fig. 6 in the appendix).

As discussed in Sec. II and III, the multiple solutions at the

G_0W_0 @PBE level of theory are an artifact caused by the lack of eigenvalue self-consistency in G . Therefore, we should disregard the unphysical multi-solution G_0W_0 @PBE calculations and instead investigate whether we can obtain numerically precise $\text{ev}G_0W_0$ HOMO QP energies using low-scaling GW. [28, 33] [33]

VIII. NUMERICALLY PRECISE LOW-SCALING $\text{ev}G_0W_0$ CALCULATIONS ON O_3 , BeO, MgO, BN, CuCN

Following the discussion in Sec. III, $\text{ev}G_0W_0$ @PBE ensures that poles of the self-energy are separated from frontier QP energies. This cures the unphysical and numerically challenging multi-solution issue of the HOMO at the G_0W_0 @PBE level and we thus explore $\text{ev}G_0W_0$ to calculate the spectral function of the five molecules O_3 , BeO, MgO, BN, CuCN. The spectral function A_{HOMO} for the MgO molecule at the $\text{ev}G_0W_0$ @PBE level is shown in Fig. 2(d). Only a single QP peak in the spectral function is present at $\omega = 8.03$ eV. The QP peak computed from the low-scaling algorithm [134] and the CD [27] match in position (within 9 meV) and spectral weight (within 1 %, Table II).

We investigate the drastic difference between the spectral function computed with G_0W_0 and $\text{ev}G_0W_0$ by inspecting the respective self-energies, Fig. 2(a) and (b). For the $\text{ev}G_0W_0$ self-energy [Fig. 2(b)] the poles are shifted by ~ 2 eV towards lower energy compared to the G_0W_0 self-energy [Fig. 2(a)]. The $\text{ev}G_0W_0$ self-energy does not exhibit poles at the HOMO QP energy of 8.03 eV [Fig. 2(b)]. This is expected, as for $\text{ev}G_0W_0$, self-energy poles are separated from the HOMO QP energy by at least the lowest RPA excitation energy Ω_1^{RPA} , as discussed in Sec. III. The consequence is that there is only a single crossing point of the self-energy and the dashed straight line $f(\omega)$, Eq. (8), close to $\omega = 8.03$ eV. The slope of the self-energy is small at this crossing point such that the associated spectral weight is close to one. The same is observed for the other four molecules (Fig. 7 in the appendix).

We report the total spectral function $A(\omega)$ for all five challenging molecules, O_3 , BeO, MgO, BN, CuCN, from $\text{ev}G_0W_0$ in Fig. 3. For all molecules, the HOMO peak positions of low-scaling GW [134] and CD [27] agree well, the mean absolute deviation is only 12 meV (Table II). The width of the QP peaks differ between low-scaling GW and the CD; the reason is the inherently different definition of the broadening parameter η in the two algorithms, cf. Eq. (5) and Ref. 27.

Our work shows that low-scaling space-time $\text{ev}G_0W_0$ @PBE is numerically precise for O_3 , BeO, MgO, BN, CuCN. The improvement compared to the G_0W_0 @PBE is due to the fact that $\text{ev}G_0W_0$ @PBE yields well-defined QP valence peaks, whereas G_0W_0 @PBE exhibits unphysical, erroneous multi-solution behaviour as discussed in Sec. II and III. The failure of G_0W_0 @PBE also reflects in Table II: $\text{ev}G_0W_0$ @PBE HOMO energies show significantly better agreement with CCSD(T) calculations and experimental ionization potentials compared to G_0W_0 @PBE HOMO energies. Therefore, it is not reasonable to invest effort in developing low-scaling GW methods which can recover the G_0W_0 @PBE solution

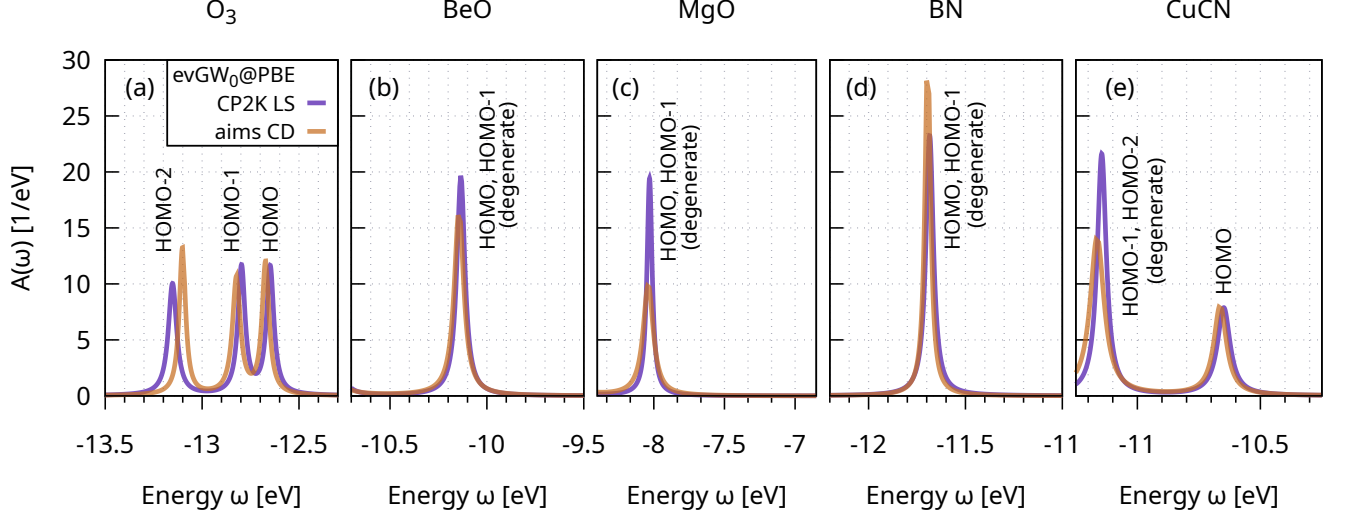


FIG. 3. (a)-(e) $evGW_0@PBE$ spectral function for five numerically challenging molecules (O_3 , BeO , MgO , BN , $CuCN$) computed from low-scaling GW [134] (CP2K LS) and from CD [27] (aims CD). Peak positions and spectral weight of the HOMO peaks are listed in Table II. $G_0W_0@PBE$ and $G_0W_0@PBE0$ spectral functions are shown in Fig. 4 and 5. Graphical solutions of the QP equation (7) are also shown in the appendix, Fig. 6, 7 and 8 for $G_0W_0@PBE$, $evGW_0@PBE$, and $G_0W_0@PBE0$, respectively.

TABLE II. $evGW_0@PBE$ HOMO energy, $\epsilon_{HOMO}^{evGW_0@PBE}$ and spectral weight Z_{HOMO} of the HOMO peak, computed from CD [27] and from low-scaling (LS) GW [134] for the five multi-solution cases from the $GW100$ set using a def2-QZVP basis set. The spectral weight Z has been computed according to Eq. (A4). As comparison, we also show the $G_0W_0@PBE$ HOMO energy [5], the CCSDT(T) ionization potential [200] (computed using a def2-TZVPP basis set) and the experimental vertical ionization potential (IP).

	O_3	BeO	MgO	BN	$CuCN$
$ \epsilon_{HOMO}^{evGW_0@PBE} $ (CD)	12.667	10.141	8.039	11.695	10.663
$ \epsilon_{HOMO}^{evGW_0@PBE} $ (LS)	12.649	10.134	8.030	11.685	10.649
Z_{HOMO} (CD)	0.83	0.85	0.68	0.85	0.79
Z_{HOMO} (LS)	0.88	0.78	0.68	0.85	0.80
$ \epsilon_{HOMO}^{G_0W_0@PBE} $ [5]	11.39	8.62	6.66	11.01	9.42
CCSD(T) [200]	12.55	9.94	7.49	11.89	10.85
IP (exp.)	12.73 [5]	10.10 [5]	8.01 [201]	–	–

for these five molecules, as it is an insufficient level of theory from the outset. It was also shown for solids that $evGW_0@PBE$ outperforms $G_0W_0@PBE$ for computing accurate bandgaps, see discussion in Refs. [83] and [2, p. 29]. $evGW_0@PBE$ is thus suitable for both molecules and solids making it ideal for studying complex, disordered systems such as molecules on surfaces or interfaces. In case of issues related to PBE orbitals used in $evGW_0@PBE$, one might also refer to $evGW_0@HSE06$ [202][203] for complex systems. [33, 168].

Another way of partial self-consistency is the $evGW$ scheme. Our low-scaling algorithm is also expected to re-

produce $evGW@PBE$ results well since the multi-solution issue is resolved by eigenvalue self-consistency in G . However, $evGW@PBE$ tends to underscreen, a phenomenon that is less noticeable for molecular frontier orbitals but becomes more apparent for deeper states [33]. This underscreening is particularly evident in solids, where it has been shown that $evGW@PBE$ produces bandgaps that are too large compared to experimental values [2, 83]. The effectiveness of $evGW_0@PBE$ arises from a fortunate error cancellation: while the PBE approximation typically underestimates the fundamental gap, using PBE eigenvalues in W leads to an overscreened potential. This overscreening in W counteracts the underscreening caused by the absence of vertex corrections, which is another way of expressing the analysis in Appendix B.

IX. NUMERICALLY PRECISE LOW-SCALING $G_0W_0@PBE0$ CALCULATIONS ON O_3 , BeO , MgO , BN , $CuCN$

The HOMO QP energies at the $G_0W_0@PBE0$ level are given in Table III. The low-scaling algorithm reproduces the QP energies from CD within 9 meV and the spectral weights within 0.01. The total spectral functions $A(\omega)$ displayed in Fig. 5 follows also closely the CD reference. This alignment occurs because the poles in the real part of Σ_{HOMO}^c shift by 2–3 eV towards more negative frequencies (Fig. 8 in the appendix), similar to what is observed in $evGW_0@PBE$ calculations. This shift is attributed to the fact that ϵ_i^{DFT} (i : occ. index) are more negative at the PBE0 than the PBE level, and Ω_s^{RPA} also increases, see Table I. The pole positions $\epsilon_i^{DFT} - \Omega_s^{RPA}$ are thus moving to the left on our en-

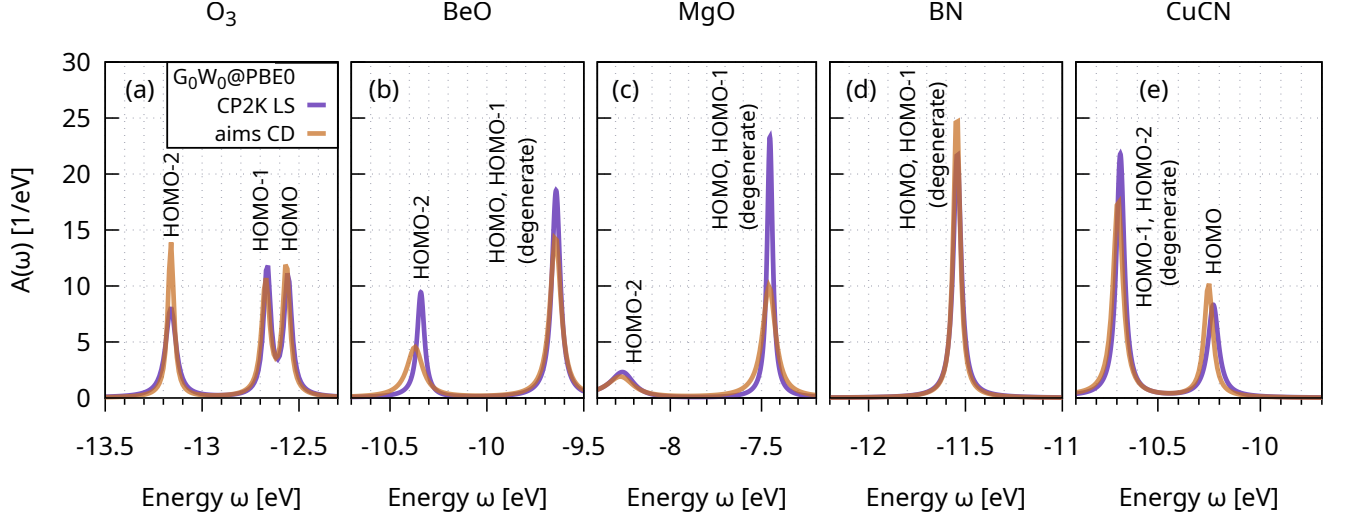


FIG. 4. (a)-(e) G_0W_0 @PBE0 spectral function for O_3 , BeO, MgO, BN, CuCN computed from low-scaling GW in CP2K [134] (CP2K LS) and from CD in FHI-aims [27] (aims CD).

ergy scale. The pole at -6.91 eV, which was the culprit for the two solutions at the G_0W_0 @PBE level, shifts now to $\epsilon_{HOMO-2}^{PBE0} - \Omega_s^{RPA@PBE0} = -9.70$ eV. A proper separation between satellite and QP peak is consequently also achieved at the G_0W_0 @PBE0 level and we obtain also a unique QP solution for all five molecules. This confirms the observation from our $evGW_0$ @PBE study from Sec. VIII: our low-scaling GW algorithm [134] is numerically precise if a well-defined QP peak is present.

G_0W_0 calculations starting from a hybrid functional with a larger fraction of exchange is common for molecules [2]. It was shown that 25% of exact exchange, as used in PBE0, is optimal to minimize the deviation from CCSD(T) for frontier orbitals [153]. However, for our five molecules, the G_0W_0 @PBE0 QP energies reported in Table III show worse agreement with CCSD(T) and experimental ionization potentials (Table II) compared to $evGW_0$ @PBE. In addition, the G_0W_0 @PBE0 approach is not extendable beyond molecular frontier orbitals: For deeper states, the amount of exact exchange needs to be progressively increased as excitation energies increase [28, 204]. For solids, G_0W_0 @PBE0 overestimates band gaps by more than 0.5 eV [205]. The

G_0W_0 @PBE0 behavior can be traced to the overestimation of excitation energies Ω_s of many-electron systems at the RPA@PBE0 level, see Table I, Appendix B and the discussion in the literature, for example in Ref. [2]. Since $\Omega_s^{RPA@PBE0}$ energies are too large, the poles in the self-energy are shifted approximately to the same frequency range as for $evGW_0$ @PBE in case of the HOMO. However, it also leads to an under-screening in W , which affects the long-range interactions in solids more significantly than in finite molecular systems.

X. CONCLUSION

In summary, our study revisits low-scaling GW calculations on molecules O_3 , BeO, MgO, BN, and CuCN from the $GW100$ benchmark set. Previous studies [134, 149] encountered numerical challenges, particularly with the computation of the G_0W_0 @PBE HOMO energy for these molecules from low-scaling GW . These challenges arise from unphysical, erroneous multiple solutions of the quasiparticle equation at the G_0W_0 @PBE level, which can be traced back to an insufficient separation between quasiparticle peak and satellite positions caused by the too high PBE eigenvalues of occupied Kohn-Sham orbitals and the lack of eigenvalue-selfconsistency in G . This suggests that G_0W_0 @PBE calculations of the HOMO of O_3 , BeO, MgO, BN, and CuCN should be disregarded. Applying self-consistency in the Green's function ($evGW_0$) or using a hybrid functional as starting point for the G_0W_0 calculation separates QP peak and satellite leading to a single HOMO QP peak and small satellite weights. Low-scaling GW computations yield numerically precise $evGW_0$ and G_0W_0 @PBE0 HOMO energies of O_3 , BeO, MgO, BN, and CuCN, with a mean absolute deviation in the order of only 10 meV from reference calculations. We thus demonstrate that low-scaling GW is well-suited for computing frontier quasiparticle energies.

TABLE III. G_0W_0 @PBE0 HOMO energy, $\epsilon_{HOMO}^{G_0W_0@PBE0}$ and spectral weight Z_{HOMO} of the HOMO peak, computed from CD [27] and from low-scaling (LS) GW [134] for all five difficult molecules from the $GW100$ set using a def2-QZVP basis set. The spectral weight Z has been computed according to Eq. (A4).

	O_3	BeO	MgO	BN	CuCN
$ \epsilon_{HOMO}^{G_0W_0@PBE0} $ (CD)	12.566	9.646	7.459	11.545	10.253
$ \epsilon_{HOMO}^{G_0W_0@PBE0} $ (LS)	12.557	9.643	7.454	11.542	10.230
Z_{HOMO} (CD)	0.81	0.76	0.67	0.83	0.81
Z_{HOMO} (LS)	0.81	0.77	0.67	0.83	0.81

DATA AVAILABILITY

Inputs and outputs of all calculations reported in this work are available in a NOMAD repository [206] and in a Github repository [207]. The low-scaling GW algorithm [134] used in this work is available in the open-source package CP2K [180, 181].

ACKNOWLEDGMENTS

This work has been supported by the Innovation Study Exa4GW. Innovation Study Exa4GW has received funding through the Inno4scale project, which is funded by the European High-Performance Computing Joint Undertaking (JU) under Grant Agreement No 101118139. The JU receives support from the European Union's Horizon Europe Programme. D.G. and J.W. acknowledge the Deutsche Forschungsgemeinschaft (DFG, German Research Foundation) for funding via the Emmy Noether Programme (Project No. 453275048 and 503985532, respectively). The authors gratefully acknowledge the computing time provided to them on the high performance computer Noctua 2 at the NHR Center PC2. These are funded by the Federal Ministry of Education and Research and the state governments participating on the basis of the resolutions of the GWK for the national high-performance computing at universities (www.nhr-verein.de/unsere-partner).

APPENDIX

Appendix A: Spectral function and spectral weight

In this appendix, we derive Eq. (9) for the spectral weight Z_ε associated with a peak at energy ε of $A_n(\omega)$. The spectral weight is the integral of that peak,

$$Z_\varepsilon = \int_{\varepsilon-\Delta}^{\varepsilon+\Delta} A_n(\omega) d\omega \quad (\text{A1})$$

$$= \int_{\varepsilon-\Delta}^{\varepsilon+\Delta} \frac{1}{\pi} \frac{|\gamma|}{(\omega - (\varepsilon + \text{Re}(\Sigma_n^c(\omega) - \Sigma_n^c(\varepsilon)))^2 + |\gamma|^2)} d\omega. \quad (\text{A2})$$

We use $\gamma = \text{Im}\Sigma_n^c(\omega) + \eta$ and we integrate over the interval $[\varepsilon - \Delta, \varepsilon + \Delta]$ with a parameter $\Delta > 0$ to exclude other peaks from the integration. We have used Eq. (5) and the QP equation (7) to arrive at the denominator in Eq. (A2).

To evaluate the integral (A2), we assume that $\text{Im}\Sigma_n^c(\omega)$ is independent of frequency and we use Taylor expansion of $\text{Re}\Sigma_n^c(\omega)$ around $\omega = \varepsilon$,

$$\text{Re}[\Sigma_n^c(\omega) - \Sigma_n^c(\varepsilon)] \approx \text{Re} \left. \frac{\partial \Sigma_n^c(\omega)}{\partial \omega} \right|_{\omega=\varepsilon} \cdot (\omega - \varepsilon). \quad (\text{A3})$$

Carrying out the integration (A2) gives the common approximate expression for the spectral weight,

$$Z_\varepsilon \approx \left[1 - \text{Re} \left. \frac{\partial \Sigma_n^c(\omega)}{\partial \omega} \right|_{\omega=\varepsilon} \right]^{-1}.$$

In practice, for Table II and III, we determine the spectral weight Z of a peak in $A_{\text{HOMO}}(\omega)$ by fitting a Lorentz function

$$L(\omega) = Z \cdot \frac{1}{\pi} \frac{\gamma}{(\omega - \varepsilon_n^{G_0W_0})^2 + \gamma^2} \quad (\text{A4})$$

to $A_{\text{HOMO}}(\omega)$. We fix the position of the peak as the solution of the QP equation $\varepsilon_n^{G_0W_0}$, while the peak width γ and the spectral weight Z were fitted.

Note that in non-selfconsistent GW flavors like G_0W_0 or $\text{ev}G_0W_0$, the particle number is not conserved [171]. The violation is often in the order of 1 % or less [171]. For fully self-consistent GW, the particle number is conserved, i.e., $\int_{-\infty}^{\infty} A_n^{GW}(\omega) d\omega = 1$.

Appendix B: Excitation energies Ω_s from Casida's equations

In TDDFT, Casida's equations [160, 208] provide a framework for calculating electronic excitation energies Ω_s . Casida's formalism casts the TDDFT linear response problem into an eigenvalue problem,

$$\begin{pmatrix} \mathbf{A} & \mathbf{B} \\ -\mathbf{B} & -\mathbf{A} \end{pmatrix} \begin{pmatrix} \mathbf{X}_s \\ \mathbf{Y}_s \end{pmatrix} = \Omega_s^{\text{TDDFT}} \begin{pmatrix} \mathbf{X}_s \\ \mathbf{Y}_s \end{pmatrix}, \quad (\text{B1})$$

where Ω_s^{TDDFT} are the excitation energies, i.e., the energy difference of an excited-state energy and the ground-state energy. $(\mathbf{X}_s, \mathbf{Y}_s)$ are the eigenvectors of the excitation. The matrix elements of \mathbf{A} and \mathbf{B} are given by

$$A_{ia,jb} = (\varepsilon_a^{\text{DFT}} - \varepsilon_i^{\text{DFT}}) \delta_{ij} \delta_{ab} + \langle ia | f_{\text{Hxc}} | jb \rangle, \quad (\text{B2})$$

$$B_{ia,jb} = \langle ia | f_{\text{Hxc}} | bj \rangle, \quad (\text{B3})$$

where $\varepsilon_i^{\text{DFT}}$ and $\varepsilon_a^{\text{DFT}}$ are KS orbital energies, δ_{ij} and δ_{ab} are Kronecker deltas and $f_{\text{Hxc}} = f_{\text{H}} + f_{\text{xc}}$ is the Hartree-exchange-correlation kernel, which includes both the Hartree and exchange-correlation (xc) kernel.

TDDFT in Casida's formulation is exact in case the exact xc kernel is used. In practice one relies on approximations, for example the adiabatic local-density approximation [160], the PBE functional [151] or the PBE0 functional [209]. This is important in GW calculations as the self-energy (2) depends on excitation energies. For small molecules, excitation energies Ω_s^{TDDFT} computed from one of these approximations are often quite similar [160]; for MgO, we have

$$\Omega_1^{\text{PBE}} = 0.67 \text{ eV} \approx \Omega_1^{\text{PBE0}} = 0.62 \text{ eV}, \quad (\text{B4})$$

see also Table I. In contrast, the HOMO-LUMO gaps of PBE and PBE0 differ substantially; we have for the MgO molecule

$$\varepsilon_{\text{LUMO}}^{\text{PBE}} - \varepsilon_{\text{HOMO}}^{\text{PBE}} = 0.50 \text{ eV}, \quad (\text{B5})$$

$$\varepsilon_{\text{LUMO}}^{\text{PBE0}} - \varepsilon_{\text{HOMO}}^{\text{PBE0}} = 2.47 \text{ eV}. \quad (\text{B6})$$

To better understand $\Omega_1^{\text{PBE}} \approx \Omega_1^{\text{PBE0}}$ and the big difference of the PBE and PBE0 HOMO-LUMO gap, we focus on large Coulomb interactions of densities with non-zero charge,

$$\langle nn|V|mm\rangle = \int d\mathbf{r}d\mathbf{r}' \frac{|\psi_n(\mathbf{r})|^2 |\psi_m(\mathbf{r}')|^2}{|\mathbf{r} - \mathbf{r}'|}, \quad (\text{B7})$$

that are present in the exact-exchange part of PBE0. For an occupied orbital i , the exact-exchange part of PBE0 contains the large interaction

$$\Delta_i = \beta \langle ii|V|ii\rangle \quad (\text{B8})$$

where $\beta = 0.25$ for PBE0. Δ_i reduces occupied KS orbital energies of small molecules in PBE0 compared to PBE,

$$\epsilon_i^{\text{PBE0}} \approx \epsilon_i^{\text{PBE}} - \Delta_i. \quad (\text{B9})$$

This reduction of occupied orbital energies in PBE0 is a primary contribution to the increased HOMO-LUMO gap in PBE0 compared to PBE.

Excitation energies from PBE and PBE0 are similar for small molecules, Eq. (B4). We trace this finding back to the diagonal matrix elements of $A_{ia,ia}$, Eq. (B2). In PBE, we have $\langle ia|f_{\text{Hxc}}^{\text{PBE}}|ia\rangle \approx 0$, such that $A_{ia,ia} \approx \epsilon_a^{\text{PBE}} - \epsilon_i^{\text{PBE}}$. In PBE0, we have for small molecules [160]

$$\langle ia|f_{\text{Hxc}}^{\text{PBE0}}|ia\rangle \approx -\beta \langle ii|V|aa\rangle \quad (\text{B10})$$

where $-\langle ii|V|aa\rangle$ is the Coulomb interaction of an electron in a previously empty orbital $\psi_a(\mathbf{r})$ with a hole in a previously occupied orbital $\psi_i(\mathbf{r})$. In case orbitals are delocalized over the whole molecule, the Coulomb interaction $\langle ii|V|aa\rangle$ is similar to the Coulomb interaction of $\psi_i(\mathbf{r})$ with itself, $\langle ii|V|aa\rangle \approx \langle ii|V|ii\rangle$. This allows us to use definition (B8)

$$\langle ia|f_{\text{Hxc}}^{\text{PBE0}}|ia\rangle \approx -\Delta_i, \quad (\text{B11})$$

such that we can estimate

$$A_{ia,ia}^{\text{PBE0}} \approx \epsilon_a^{\text{PBE0}} - \epsilon_i^{\text{PBE0}} - \Delta_i \approx \epsilon_a^{\text{PBE}} - \epsilon_i^{\text{PBE}} \approx A_{ia,ia}^{\text{PBE}}. \quad (\text{B12})$$

Our estimate (B12) rationalizes $\Omega_1^{\text{PBE}} \approx \Omega_1^{\text{PBE0}}$, Eq. (B4).

Equation (B12) can be also understood by recognizing that the self-interaction in the HOMO level of KS-DFT and the absence of electron-hole Coulomb interaction in the xc kernel have similar magnitudes but opposite signs, leading to a mutual cancellation.

One often employs the RPA in *GW*, mainly for computational efficiency. In RPA, the xc kernel f_{xc} is neglected in Casida's equations,

$$\begin{pmatrix} \mathbf{A}^{\text{RPA}} & \mathbf{B}^{\text{RPA}} \\ -\mathbf{B}^{\text{RPA}} & -\mathbf{A}^{\text{RPA}} \end{pmatrix} \begin{pmatrix} \mathbf{X}_s^{\text{RPA}} \\ \mathbf{Y}_s^{\text{RPA}} \end{pmatrix} = \Omega_s^{\text{RPA}} \begin{pmatrix} \mathbf{X}_s^{\text{RPA}} \\ \mathbf{Y}_s^{\text{RPA}} \end{pmatrix}, \quad (\text{B13})$$

$$A_{ia,jb}^{\text{RPA}} = (\epsilon_a^{\text{DFT}} - \epsilon_i^{\text{DFT}}) \delta_{ij} \delta_{ab} + \langle ia|f_{\text{H}}|jb\rangle, \quad (\text{B14})$$

$$B_{ia,jb}^{\text{RPA}} = \langle ia|f_{\text{H}}|bj\rangle. \quad (\text{B15})$$

When using the PBE functional, RPA leaves the diagonal elements of \mathbf{A} almost unchanged because $\langle ia|f_{\text{xc}}^{\text{PBE}}|ia\rangle \approx 0$,

$$A_{ia,ia}^{\text{RPA@PBE}} \approx \epsilon_a^{\text{PBE}} - \epsilon_i^{\text{PBE}} \approx A_{ia,ia}^{\text{PBE}} \approx A_{ia,ia}^{\text{PBE0}}. \quad (\text{B16})$$

Thus, PBE excitation energies change only little under RPA; for the MgO molecule, we have

$$\Omega_1^{\text{RPA@PBE}} = 0.82 \text{ eV} \approx \Omega_1^{\text{PBE}} = 0.67 \text{ eV}. \quad (\text{B17})$$

When applying the RPA with the PBE0 functional, the diagonal elements of \mathbf{A} increase by $\approx \Delta_i$:

$$A_{ia,ia}^{\text{RPA@PBE0}} \stackrel{(\text{B14}),(\text{B12})}{\approx} \epsilon_a^{\text{PBE0}} - \epsilon_i^{\text{PBE0}} \approx A_{ia,ia}^{\text{PBE0}} + \Delta_i. \quad (\text{B18})$$

This increase translates to spuriously increased excitation energies in RPA@PBE0; again, for MgO, we have

$$\Omega_1^{\text{RPA@PBE0}} = 2.83 \text{ eV} \gg \Omega_1^{\text{PBE0}} = 0.62 \text{ eV}, \quad (\text{B19})$$

see also Table I.

RPA excitation energies are used in the *GW* self-energy, see Eq. (2). It has already long been recognized that starting a G_0W_0 calculation from PBE0 features too large RPA@PBE0 excitation energies [2], see Eq. (B19) as an example. It is often recommended to use the PBE functional as starting point for *GW* calculations because of $\Omega_s^{\text{RPA@PBE}} \approx \Omega_s^{\text{PBE}}$. To cure the too high PBE eigenvalues of occupied KS orbitals in *G*, Eq. (2), it is often recommended to use *evGW*₀@PBE [2].

Appendix C: Self-energy and spectral function of all molecules O₃, BeO, MgO, BN, CuCN

We provide spectral function $A(\omega)$ of the previously challenging five molecules O₃, BeO, MgO, BN, CuCN computed from G_0W_0 @PBE (Fig. 5). We also show $\text{Re}(\Sigma_{\text{HOMO}}^c)$, $\text{Im}(\Sigma_{\text{HOMO}}^c)$ and A_{HOMO} [Eq. (5)] for O₃, BeO, MgO, BN and CuCN computed from G_0W_0 @PBE, *evGW*₀@PBE and G_0W_0 @PBE0 (Fig. 6, 7 and 8).

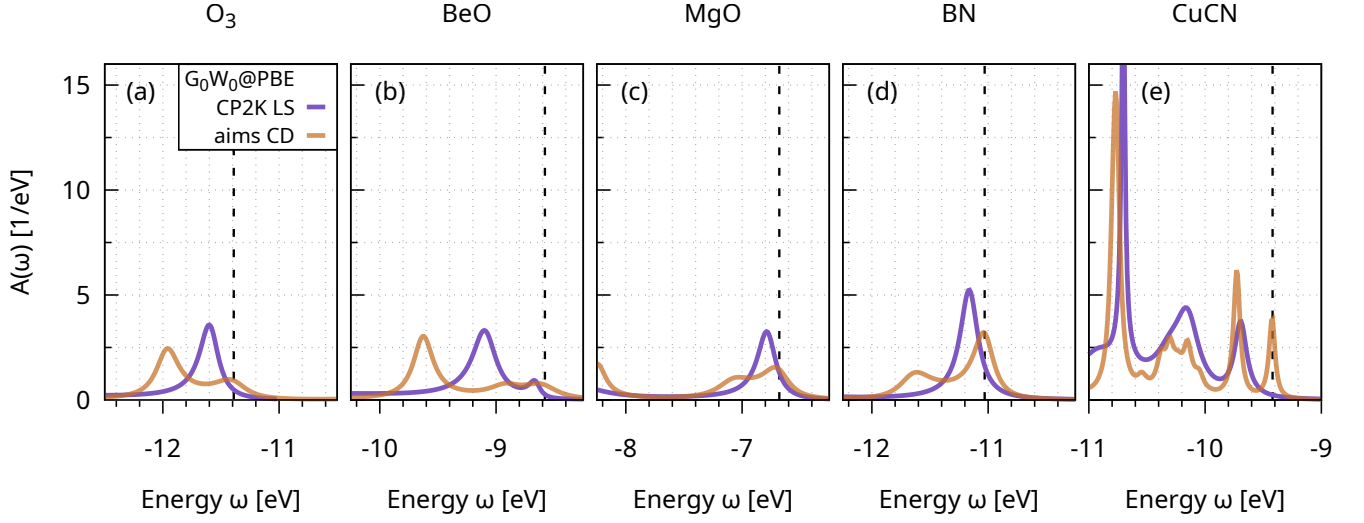


FIG. 5. (a)-(e) G_0W_0 @PBE spectral function for O_3 , BeO, MgO, BN, CuCN computed from low-scaling GW in CP2K [134] (CP2K LS) and from CD in FHI-aims [27] (aims CD). The dashed lines indicate the G_0W_0 @PBE HOMO energy computed from FHI-aims and 128-parameter Padé continuation taken from the original GW100 work [5].

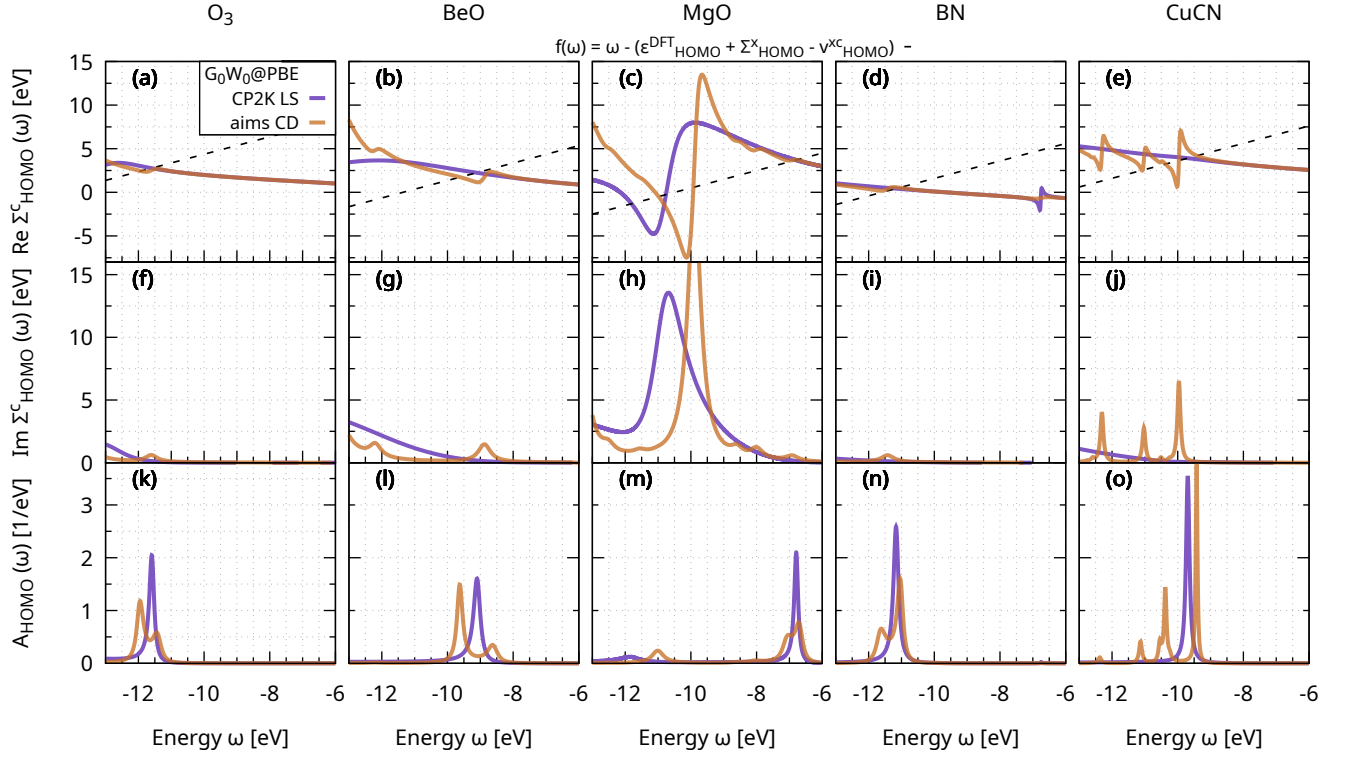


FIG. 6. (a)-(e) $\text{Re}(\Sigma_{\text{HOMO}}^c)$, (f)-(j) $\text{Im}(\Sigma_{\text{HOMO}}^c)$, (k)-(o) A_{HOMO} [Eq. (5)] for O_3 , BeO, MgO, BN and CuCN computed from G_0W_0 @PBE.

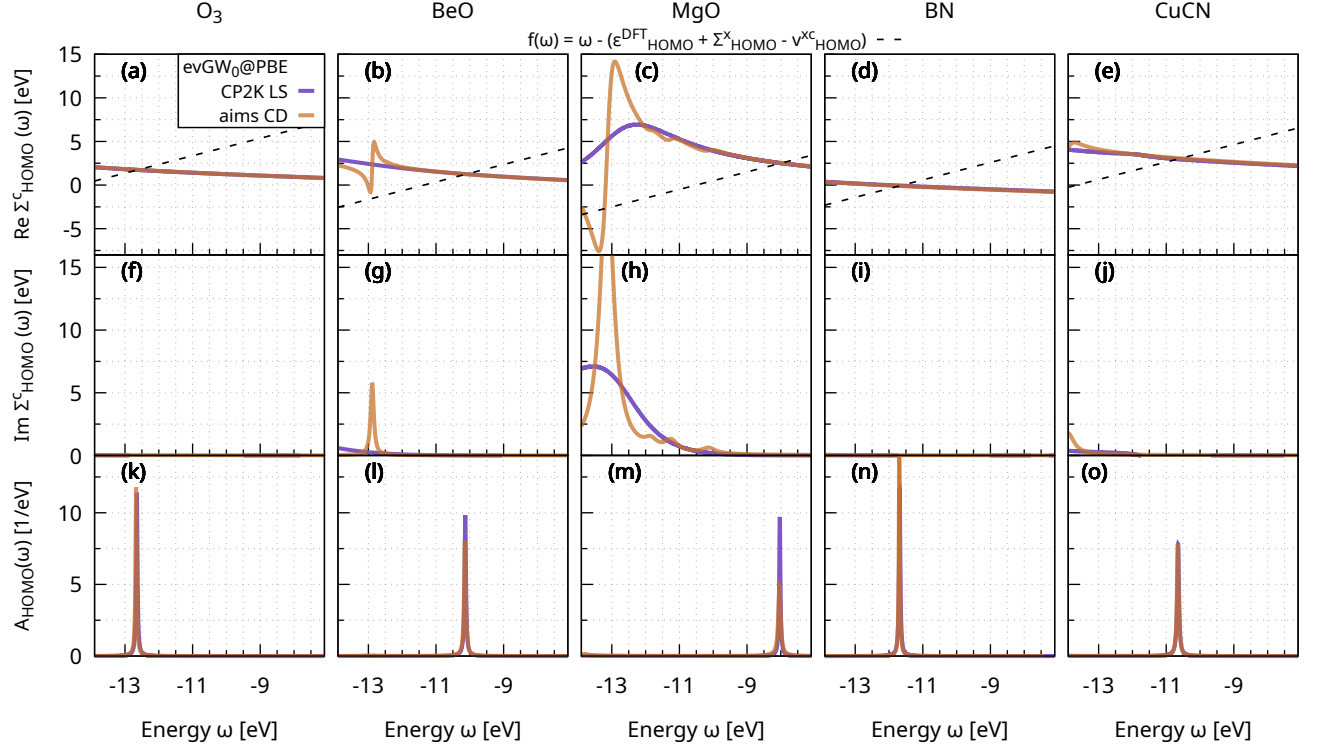


FIG. 7. (a)-(e) $\text{Re}(\Sigma_{\text{HOMO}}^c)$, (f)-(j) $\text{Im}(\Sigma_{\text{HOMO}}^c)$, (k)-(o) A_{HOMO} [Eq. (5)] for O_3 , BeO, MgO, BN and CuCN computed from $\text{evGW}_0@PBE$.

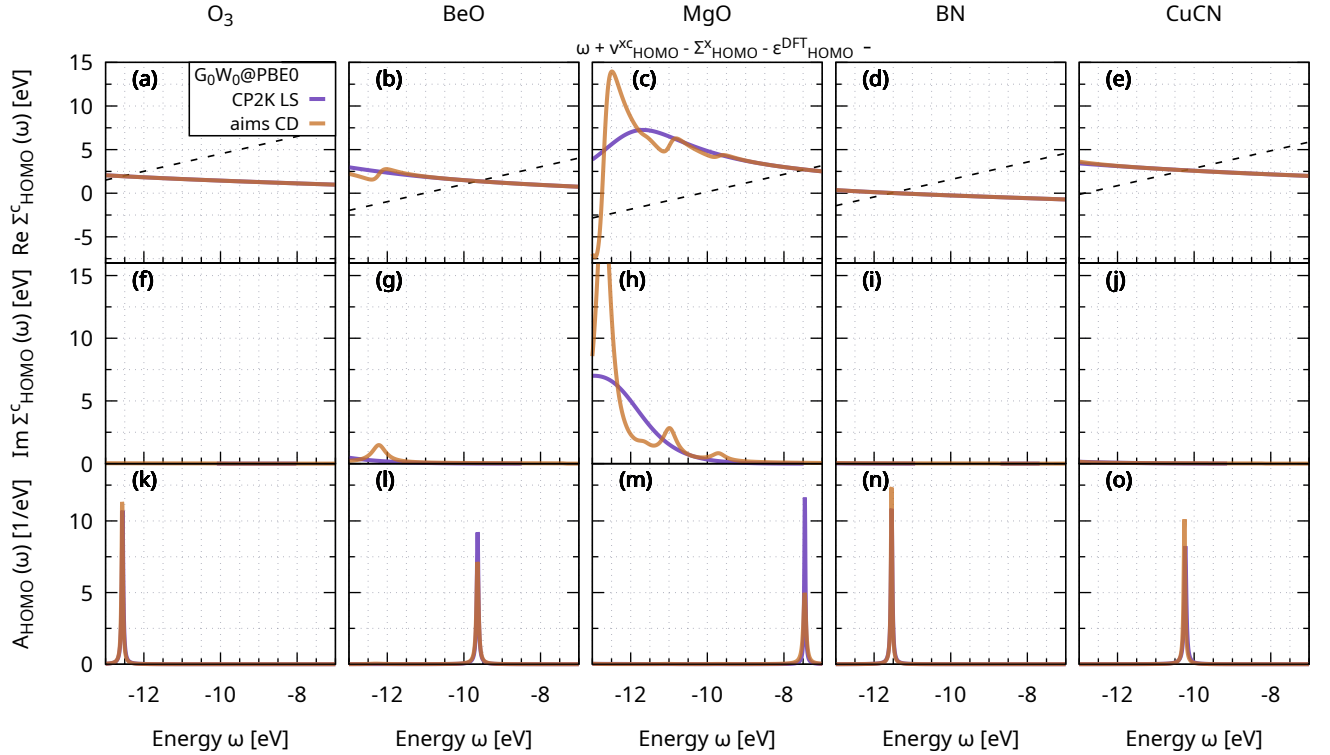


FIG. 8. (a)-(e) $\text{Re}(\Sigma_{\text{HOMO}}^c)$, (f)-(j) $\text{Im}(\Sigma_{\text{HOMO}}^c)$, (k)-(o) A_{HOMO} [Eq. (5)] for O_3 , BeO, MgO, BN and CuCN computed from $G_0W_0@PBE0$.

- [1] L. Hedin, New method for calculating the one-particle Green's function with application to the electron-gas problem, *Phys. Rev.* **139**, A796 (1965).
- [2] D. Golze, M. Dvorak, and P. Rinke, The GW Compendium: A Practical Guide to Theoretical Photoemission Spectroscopy, *Front. Chem.* **7**, 377 (2019).
- [3] L. Reining, The GW approximation: content, successes and limitations, *Wiley Interdiscip. Rev. Comput. Mol. Sci.* **8**, e1344 (2018).
- [4] X. Blase, C. Attaccalite, and V. Olevano, First-principles GW calculations for fullerenes, porphyrins, phthalocyanine, and other molecules of interest for organic photovoltaic applications, *Phys. Rev. B* **83**, 115103 (2011).
- [5] M. J. van Setten, F. Caruso, S. Sharifzadeh, X. Ren, M. Scheffler, F. Liu, J. Lischner, L. Lin, J. R. Deslippe, S. G. Louie, C. Yang, F. Weigend, J. B. Neaton, F. Evers, and P. Rinke, GW100: Benchmarking G_0W_0 for Molecular Systems, *J. Chem. Theory Comput.* **11**, 5665 (2015).
- [6] J. W. Knight, X. Wang, L. Gallandi, O. Dolgounitcheva, X. Ren, J. V. Ortiz, P. Rinke, T. Körzdörfer, and N. Marom, Accurate Ionization Potentials and Electron Affinities of Acceptor Molecules III: A Benchmark of GW Methods, *J. Chem. Theory Comput.* **12**, 615 (2016).
- [7] A. Molina-Sánchez, D. Sangalli, K. Hummer, A. Marini, and L. Wirtz, Effect of spin-orbit interaction on the optical spectra of single-layer, double-layer, and bulk MoS_2 , *Phys. Rev. B* **88**, 045412 (2013).
- [8] W. Xia, W. Gao, G. Lopez-Candales, Y. Wu, W. Ren, W. Zhang, and P. Zhang, Combined subsampling and analytical integration for efficient large-scale GW calculations for 2D systems, *npj Comput. Mater.* **6**, 118 (2020).
- [9] M. N. Gjerding, A. Taghizadeh, A. Rasmussen, S. Ali, F. Bertoldo, T. Deilmann, N. R. Knøsgaard, M. Kruse, A. H. Larsen, S. Manti, T. G. Pedersen, U. Petralanda, T. Skovhus, M. K. Svendsen, J. J. Mortensen, T. Olsen, and K. S. Thygesen, Recent progress of the Computational 2D Materials Database (C2DB), *2D Mater.* **8**, 044002 (2021).
- [10] A. Rasmussen, T. Deilmann, and K. S. Thygesen, Towards fully automated GW band structure calculations: What we can learn from 60.000 self-energy evaluations, *npj Comput. Mater.* **7**, 22 (2021).
- [11] E. Mitterreiter, B. Schuler, A. Micevic, D. Hernangómez-Pérez, K. Barthelmi, K. A. Cochran, J. Kiemle, F. Sigger, J. Klein, E. Wong, E. S. Barnard, K. Watanabe, T. Taniguchi, M. Lorke, F. Jahnke, J. J. Finley, A. M. Schwartzberg, D. Y. Qiu, S. Refaely-Abramson, A. W. Holleitner, A. Weber-Bargioni, and C. Kastl, The role of chalcogen vacancies for atomic defect emission in MoS_2 , *Nat. Commun.* **12**, 3822 (2021).
- [12] K.-Q. Lin, C. S. Ong, S. Bange, P. E. Faria Junior, B. Peng, J. D. Ziegler, J. Zipfel, C. Bäuml, N. Paradiso, K. Watanabe, T. Taniguchi, C. Strunk, B. Monserrat, J. Fabian, A. Chernikov, D. Y. Qiu, S. G. Louie, and J. M. Lupton, Narrow-band high-lying excitons with negative-mass electrons in monolayer WSe_2 , *Nat. Commun.* **12**, 5500 (2021).
- [13] A. Guandalini, P. D'Amico, A. Ferretti, and D. Varsano, Efficient GW calculations in two dimensional materials through a stochastic integration of the screened potential, *npj Comput. Mater.* **9**, 44 (2023).
- [14] M. Graml, K. Zollner, D. Hernangómez-Pérez, P. E. Faria Junior, and J. Wilhelm, Low-Scaling GW Algorithm Applied to Twisted Transition-Metal Dichalcogenide Heterobilayers, *J. Chem. Theory Comput.* **20**, 2202 (2024).
- [15] M. Camarasa-Gómez, A. Ramasubramaniam, J. B. Neaton, and L. Kronik, Transferable screened range-separated hybrid functionals for electronic and optical properties of van der Waals materials, *Phys. Rev. Mater.* **7**, 104001 (2023).
- [16] M. Camarasa-Gómez, S. E. Gant, G. Ohad, J. B. Neaton, A. Ramasubramaniam, and L. Kronik, Electronic and Optical Excitations in van der Waals Materials from a Non-Empirical Wannier-Localized Optimally-Tuned Screened Range-Separated Hybrid Functional (2024), [arXiv:2405.00643](https://arxiv.org/abs/2405.00643).
- [17] R. Rodrigues Pela, C. Vona, S. Lubeck, B. Alex, I. Gonzalez Oliva, and C. Draxl, Critical assessment of G_0W_0 calculations for 2D materials: the example of monolayer MoS_2 , *npj Comput. Mater.* **10**, 77 (2024).
- [18] J. Krumland and C. Cocchi, Electronic Structure of Low-Dimensional Inorganic/Organic Interfaces: Hybrid Density Functional Theory, G_0W_0 , and Electrostatic Models, *Phys. Stat. Solidi A* **221**, 2300089 (2024).
- [19] J. Krumland and C. Cocchi, Ab Initio Modeling of Mixed-Dimensional Heterostructures: A Path Forward, *J. Phys. Chem. Lett.* **15**, 5350 (2024).
- [20] F. Bruneval and X. Gonze, Accurate GW self-energies in a plane-wave basis using only a few empty states: Towards large systems, *Phys. Rev. B* **78**, 085125 (2008).
- [21] M. R. Filip, G. E. Eperon, H. J. Snaith, and F. Giustino, Steric engineering of metal-halide perovskites with tunable optical band gaps, *Nat. Commun.* **5**, 5757 (2014).
- [22] Y. Cho and T. C. Berkelbach, Optical Properties of Layered Hybrid Organic-Inorganic Halide Perovskites: A Tight-Binding GW-BSE Study, *J. Phys. Chem. Lett.* **10**, 6189 (2019).
- [23] X. Ren, F. Merz, H. Jiang, Y. Yao, M. Rampp, H. Lederer, V. Blum, and M. Scheffler, All-electron periodic G_0W_0 implementation with numerical atomic orbital basis functions: Algorithm and benchmarks, *Phys. Rev. Mater.* **5**, 013807 (2021).
- [24] R.-I. Biega, Y. Chen, M. R. Filip, and L. Leppert, Chemical Mapping of Excitons in Halide Double Perovskites, *Nano Lett.* **23**, 8155 (2023).
- [25] G. Biffi, Y. Cho, R. Krahne, and T. C. Berkelbach, Excitons and Their Fine Structure in Lead Halide Perovskite Nanocrystals from Atomistic GW/BSE Calculations, *J. Phys. Chem. C* **127**, 1891 (2023).
- [26] L. Leppert, Excitons in metal-halide perovskites from first-principles many-body perturbation theory, *J. Chem. Phys.* **160**, 050902 (2024).
- [27] D. Golze, J. Wilhelm, M. J. van Setten, and P. Rinke, Core-Level Binding Energies from GW: An Efficient Full-Frequency Approach within a Localized Basis., *J. Chem. Theory Comput.* **14**, 4856 (2018).
- [28] D. Golze, L. Keller, and P. Rinke, Accurate Absolute and Relative Core-Level Binding Energies from GW, *J. Phys. Chem. Lett.* **11**, 1840 (2020).
- [29] L. Keller, V. Blum, P. Rinke, and D. Golze, Relativistic correction scheme for core-level binding energies from GW, *J. Chem. Phys.* **153**, 114110 (2020).
- [30] T. Zhu and G. K.-L. Chan, All-Electron Gaussian-Based G_0W_0 for Valence and Core Excitation Energies of Periodic Systems, *J. Chem. Theory Comput.* **17**, 727 (2021).

- [31] D. Mejia-Rodriguez, A. Kunitsa, E. Aprà, and N. Govind, Scalable Molecular GW Calculations: Valence and Core Spectra, *J. Chem. Theory Comput.* **17**, 7504 (2021).
- [32] D. Mejia-Rodriguez, A. Kunitsa, E. Aprà, and N. Govind, Basis Set Selection for Molecular Core-Level GW Calculations, *J. Chem. Theory Comput.* **18**, 4919 (2022).
- [33] J. Li, Y. Jin, P. Rinke, W. Yang, and D. Golze, Benchmark of GW Methods for Core-Level Binding Energies, *J. Chem. Theory Comput.* **18**, 7570 (2022).
- [34] R. L. Panadés-Barrueta and D. Golze, Accelerating Core-Level GW Calculations by Combining the Contour Deformation Approach with the Analytic Continuation of W, *J. Chem. Theory Comput.* **19**, 5450 (2023).
- [35] L. Galleni, D. Escudero, G. Pourtois, and M. J. van Setten, The C1s core levels of polycyclic aromatic hydrocarbons and styrenic polymers: A first-principles study, *J. Chem. Phys.* **160**, 214105 (2024).
- [36] M. Kühn and F. Weigend, One-Electron Energies from the Two-Component GW Method, *J. Chem. Theory Comput.* **11**, 969 (2015).
- [37] C. Holzer and W. Klopper, Ionized, electron-attached, and excited states of molecular systems with spin-orbit coupling: Two-component GW and Bethe-Salpeter implementations, *J. Chem. Phys.* **150**, 204116 (2019).
- [38] C.-N. Yeh, A. Shee, Q. Sun, E. Gull, and D. Zgid, Relativistic self-consistent GW: Exact two-component formalism with one-electron approximation for solids, *Phys. Rev. B* **106**, 085121 (2022).
- [39] A. Förster, E. van Lenthe, E. Spadetto, and L. Visscher, Two-Component GW Calculations: Cubic Scaling Implementation and Comparison of Vertex-Corrected and Partially Self-Consistent GW Variants, *J. Chem. Theory Comput.* **19**, 5958 (2023).
- [40] M. Kehry, W. Klopper, and C. Holzer, Robust relativistic many-body Green's function based approaches for assessing core ionized and excited states, *J. Chem. Phys.* **159**, 044116 (2023).
- [41] H. Gaurav, A. Vibin, and D. Zgid, Challenges with relativistic GW calculations in solids and molecules, *Faraday Discuss.* (2024).
- [42] V. Abraham, G. Harsha, and D. Zgid, Relativistic fully self-consistent GW for molecules: Total energies and ionization potentials (2024), [arXiv:2401.11303](https://arxiv.org/abs/2401.11303).
- [43] O. Çaylak and B. Baumeier, Excited-State Geometry Optimization of Small Molecules with Many-Body Green's Functions Theory, *J. Chem. Theory Comput.* **17**, 879 (2021).
- [44] J. A. Berger, P.-F. Loos, and P. Romaniello, Potential Energy Surfaces without Unphysical Discontinuities: The Coulomb Hole Plus Screened Exchange Approach, *J. Chem. Theory Comput.* **17**, 191 (2021).
- [45] I. Knysh, K. Letellier, I. Duchemin, X. Blase, and D. Jacquemin, Excited state potential energy surfaces of n-phenylpyrrole upon twisting: reference values and comparison between bse/gw and td-dft, *Phys. Chem. Chem. Phys.* **25**, 8376 (2023).
- [46] I. Knysh, D. Raimbault, I. Duchemin, X. Blase, and D. Jacquemin, Assessing the accuracy of TD-DFT excited-state geometries through optimal tuning with GW energy levels, *J. Chem. Phys.* **160**, 144115 (2024).
- [47] C. Attaccalite, M. Grüning, and A. Marini, Real-time approach to the optical properties of solids and nanostructures: Time-dependent Bethe-Salpeter equation, *Phys. Rev. B* **84**, 245110 (2011).
- [48] X. Jiang, Q. Zheng, Z. Lan, W. A. Saidi, X. Ren, and J. Zhao, Real-time GW-BSE investigations on spin-valley exciton dynamics in monolayer transition metal dichalcogenide, *Sci. Adv.* **7**, eabf3759 (2021).
- [49] Y.-H. Chan, D. Y. Qiu, F. H. da Jornada, and S. G. Louie, Giant exciton-enhanced shift currents and direct current conduction with subbandgap photo excitations produced by many-electron interactions, *Proc. Natl. Acad. Sci. U.S.A.* **118**, e1906938118 (2021).
- [50] N. Schlünzen, J.-P. Joost, and M. Bonitz, Achieving the Scaling Limit for Nonequilibrium Green Functions Simulations, *Phys. Rev. Lett.* **124**, 076601 (2020).
- [51] J.-P. Joost, N. Schlünzen, and M. Bonitz, G1-G2 scheme: Dramatic acceleration of nonequilibrium Green functions simulations within the Hartree-Fock generalized Kadanoff-Baym ansatz, *Phys. Rev. B* **101**, 245101 (2020).
- [52] E. Perfetto, Y. Pavlyukh, and G. Stefanucci, Real-Time GW: Toward an Ab Initio Description of the Ultrafast Carrier and Exciton Dynamics in Two-Dimensional Materials, *Phys. Rev. Lett.* **128**, 016801 (2022).
- [53] R. Tuovinen, D. Golež, M. Eckstein, and M. A. Sentef, Comparing the generalized Kadanoff-Baym ansatz with the full Kadanoff-Baym equations for an excitonic insulator out of equilibrium, *Phys. Rev. B* **102**, 115157 (2020).
- [54] R. Tuovinen, R. van Leeuwen, E. Perfetto, and G. Stefanucci, Electronic transport in molecular junctions: The generalized Kadanoff-Baym ansatz with initial contact and correlations, *J. Chem. Phys.* **154**, 094104 (2021).
- [55] R. Tuovinen, Y. Pavlyukh, E. Perfetto, and G. Stefanucci, Time-Linear Quantum Transport Simulations with Correlated Nonequilibrium Green's Functions, *Phys. Rev. Lett.* **130**, 246301 (2023).
- [56] Y. Pavlyukh, R. Tuovinen, E. Perfetto, and G. Stefanucci, Cheers: A Linear-Scaling KBE+GKBA Code, *Phys. Status Solidi B*, 2300504 (2023).
- [57] M. Bonitz, J.-P. Joost, C. Makait, E. Schroedter, T. Kalsberger, and K. Balzer, Accelerating Nonequilibrium Green Functions Simulations: The G1-G2 Scheme and Beyond, *Phys. Status Solidi B*, 2300578 (2024).
- [58] C. C. Reeves, G. Harsha, A. Shee, Y. Zhu, C. Yang, K. B. Whaley, D. Zgid, and V. Vlček, Performance of wave function and Green's functions based methods for non equilibrium many-body dynamics (2024), [arXiv:2405.08814](https://arxiv.org/abs/2405.08814).
- [59] C. Holzer, A. M. Teale, F. Hampe, S. Stopkowicz, T. Helgaker, and W. Klopper, GW quasiparticle energies of atoms in strong magnetic fields, *J. Chem. Phys.* **150**, 214112 (2019).
- [60] C. Holzer, A. Pausch, and W. Klopper, The GW/BSE method in magnetic fields, *Front. Chem.* **9**, 746162 (2021).
- [61] Y. J. Franzke, C. Holzer, and F. Mack, NMR Coupling Constants Based on the Bethe-Salpeter Equation in the GW Approximation, *J. Chem. Theory Comput.* **18**, 1030 (2022).
- [62] C. Holzer, Practical Post-Kohn-Sham Methods for Time-Reversal Symmetry Breaking References, *J. Chem. Theory Comput.* **19**, 3131 (2023).
- [63] F. Bruneval, N. Dattani, and M. J. van Setten, The GW Miracle in Many-Body Perturbation Theory for the Ionization Potential of Molecules, *Front. Chem.* **9**, 749779 (2021).
- [64] R. Orlando, P. Romaniello, and P.-F. Loos, The three channels of many-body perturbation theory: GW, particle-particle, and electron-hole T-matrix self-energies, *J. Chem. Phys.* **159**, 184113 (2023).
- [65] S. Marek and R. Korytár, Widening of the fundamental gap in cluster GW for metal-molecular interfaces, *Phys. Chem. Chem. Phys.* **26**, 2127 (2024).

- [66] A. Ammar, A. Marie, M. Rodríguez-Mayorga, H. G. A. Burton, and P.-F. Loos, Can GW Handle Multireference Systems? (2024), [arXiv:2401.03745](#).
- [67] E. Maggio, P. Liu, M. J. van Setten, and G. Kresse, GW100: A Plane Wave Perspective for Small Molecules, *J. Chem. Theory Comput.* **13**, 635 (2017).
- [68] M. J. van Setten, M. Giantomassi, X. Gonze, G.-M. Rignanese, and G. Hautier, Automation methodologies and large-scale validation for GW: Towards high-throughput GW calculations, *Phys. Rev. B* **96**, 155207 (2017).
- [69] W. Gao and J. R. Chelikowsky, Real-Space Based Benchmark of G_0W_0 Calculations on GW100: Effects of Semicore Orbitals and Orbital Reordering, *J. Chem. Theory Comput.* **15**, 5299 (2019).
- [70] M. Govoni and G. Galli, GW100: Comparison of Methods and Accuracy of Results Obtained with the WEST Code, *J. Chem. Theory Comput.* **14**, 1895 (2018).
- [71] A. Förster and L. Visscher, GW100: A Slater-Type Orbital Perspective, *J. Chem. Theory Comput.* **17**, 5080 (2021).
- [72] T. Rangel, M. Del Ben, D. Varsano, G. Antonius, F. Bruneval, F. H. da Jornada, M. J. van Setten, O. K. Orhan, D. D. O'Regan, A. Canning, A. Ferretti, A. Marini, G.-M. Rignanese, J. Deslippe, S. G. Louie, and J. B. Neaton, Reproducibility in G_0W_0 calculations for solids, *Comput. Phys. Commun.* **255**, 107242 (2020).
- [73] A. Stuke, C. Kunkel, D. Golze, M. Todorović, J. T. Margraf, K. Reuter, P. Rinke, and H. Oberhofer, Atomic structures and orbital energies of 61,489 crystal-forming organic molecules, *Sci. Data* **7**, 1 (2020).
- [74] J. Westermayr and R. J. Maurer, Physically inspired deep learning of molecular excitations and photoemission spectra, *Chem. Sci.* **12**, 10755 (2021).
- [75] D. Golze, M. Hirvensalo, P. Hernández-León, A. Aarva, J. Etula, T. Susi, P. Rinke, T. Laurila, and M. A. Caro, Accurate Computational Prediction of Core-Electron Binding Energies in Carbon-Based Materials: A Machine-Learning Model Combining Density-Functional Theory and GW, *Chem. Mater.* **34**, 6240 (2022).
- [76] A. Fediai, P. Reiser, J. E. O. Peña, W. Wenzel, and P. Friederich, Interpretable delta-learning of GW quasiparticle energies from GGA-DFT, *Mach. Learn. Sci. Technol.* **4**, 035045 (2023).
- [77] B. Mondal, J. Westermayr, and R. Tonner-Zech, Machine learning for accelerated bandgap prediction in strain-engineered quaternary III–V semiconductors, *J. Chem. Phys.* **159**, 104702 (2023).
- [78] M. G. Zauchner, A. Horsfield, and J. Lischner, Accelerating GW calculations through machine-learned dielectric matrices, *npj Comput. Mater.* **9**, 184 (2023).
- [79] C. Venturella, C. Hillenbrand, J. Li, and T. Zhu, Machine Learning Many-Body Green's Functions for Molecular Excitation Spectra, *J. Chem. Theory Comput.* **20**, 143 (2024).
- [80] R. Del Sole, L. Reining, and R. W. Godby, GW approximation for electron self-energies in semiconductors and insulators, *Phys. Rev. B* **49**, 8024 (1994).
- [81] E. L. Shirley and R. M. Martin, GW quasiparticle calculations in atoms, *Phys. Rev. B* **47**, 15404 (1993).
- [82] F. Bruneval, F. Sottile, V. Olevano, R. Del Sole, and L. Reining, Many-Body Perturbation Theory Using the Density-Functional Concept: Beyond the GW Approximation, *Phys. Rev. Lett.* **94**, 186402 (2005).
- [83] M. Shishkin, M. Marsman, and G. Kresse, Accurate Quasiparticle Spectra from Self-Consistent GW Calculations with Vertex Corrections, *Phys. Rev. Lett.* **99**, 246403 (2007).
- [84] A. Grüneis, G. Kresse, Y. Hinuma, and F. Oba, Ionization Potentials of Solids: The Importance of Vertex Corrections, *Phys. Rev. Lett.* **112**, 096401 (2014).
- [85] E. Maggio and G. Kresse, GW Vertex Corrected Calculations for Molecular Systems, *J. Chem. Theory Comput.* **13**, 4765 (2017).
- [86] A. M. Lewis and T. C. Berkelbach, Vertex Corrections to the Polarizability Do Not Improve the GW Approximation for the Ionization Potential of Molecules, *J. Chem. Theory Comput.* **15**, 2925 (2019).
- [87] V. Vlček, Stochastic Vertex Corrections: Linear Scaling Methods for Accurate Quasiparticle Energies, *J. Chem. Theory Comput.* **15**, 6254 (2019).
- [88] A. Tal, W. Chen, and A. Pasquarello, Vertex function compliant with the Ward identity for quasiparticle self-consistent calculations beyond GW, *Phys. Rev. B* **103**, L161104 (2021).
- [89] Y. Wang, P. Rinke, and X. Ren, Assessing the $G_0W_0\Gamma_0^{(1)}$ Approach: Beyond G_0W_0 with Hedin's Full Second-Order Self-Energy Contribution, *J. Chem. Theory Comput.* **17**, 5140 (2021).
- [90] A. Förster and L. Visscher, Exploring the statically screened G3W2 correction to the GW self-energy: Charged excitations and total energies of finite systems, *Phys. Rev. B* **105**, 125121 (2022).
- [91] A. Lorin, T. Bischoff, A. Tal, and A. Pasquarello, Band alignments through quasiparticle self-consistent GW with efficient vertex corrections, *Phys. Rev. B* **108**, 245303 (2023).
- [92] F. Bruneval and A. Förster, Fully Dynamic G3W2 Self-Energy for Finite Systems: Formulas and Benchmark, *J. Chem. Theory Comput.* **20**, 3218 (2024).
- [93] M. Wen, V. Abraham, G. Harsha, A. Shee, K. B. Whaley, and D. Zgid, Comparing Self-Consistent GW and Vertex-Corrected G_0W_0 ($G_0W_0\Gamma$) Accuracy for Molecular Ionization Potentials, *J. Chem. Theory Comput.* **20**, 3109 (2024).
- [94] M. F. Lange and T. C. Berkelbach, On the Relation between Equation-of-Motion Coupled-Cluster Theory and the GW Approximation, *J. Chem. Theory Comput.* **14**, 4224 (2018).
- [95] J. Tölle and G. Kin-Lic Chan, Exact relationships between the GW approximation and equation-of-motion coupled-cluster theories through the quasi-boson formalism, *J. Chem. Phys.* **158**, 124123 (2023).
- [96] J. Tölle and G. Kin-Lic Chan, AB- G_0W_0 : A practical G_0W_0 method without frequency integration based on an auxiliary boson expansion, *J. Chem. Phys.* **160**, 164108 (2024).
- [97] J. McClain, Q. Sun, G. K.-L. Chan, and T. C. Berkelbach, Gaussian-Based Coupled-Cluster Theory for the Ground-State and Band Structure of Solids, *J. Chem. Theory Comput.* **13**, 1209 (2017).
- [98] X. Wang and T. C. Berkelbach, Excitons in Solids from Periodic Equation-of-Motion Coupled-Cluster Theory, *J. Chem. Theory Comput.* **16**, 3095 (2020).
- [99] X. Wang and T. C. Berkelbach, Absorption Spectra of Solids from Periodic Equation-of-Motion Coupled-Cluster Theory, *J. Chem. Theory Comput.* **17**, 6387 (2021).
- [100] K. Laughon, J. M. Yu, and T. Zhu, Periodic Coupled-Cluster Green's Function for Photoemission Spectra of Realistic Solids, *J. Phys. Chem. Lett.* **13**, 9122 (2022).
- [101] A. Gallo, F. Hummel, A. Irmmler, and A. Grüneis, A periodic equation-of-motion coupled-cluster implementation applied to F-centers in alkaline earth oxides, *J. Chem. Phys.* **154**, 064106 (2021).
- [102] N. Masios, A. Irmmler, T. Schäfer, and A. Grüneis, Averting the Infrared Catastrophe in the Gold Standard of Quantum Chem-

- istry, *Phys. Rev. Lett.* **131**, 186401 (2023).
- [103] P. J. Robinson, A. Rettig, H. Q. Dinh, M.-F. Chen, and J. Lee, Condensed-Phase Quantum Chemistry (2024), [arXiv:2403.13207](https://arxiv.org/abs/2403.13207).
- [104] F. Fuchs, C. Rödl, A. Schleife, and F. Bechstedt, Efficient $\mathcal{O}(N^2)$ approach to solve the Bethe-Salpeter equation for excitonic bound states, *Phys. Rev. B* **78**, 085103 (2008).
- [105] X. Blase, I. Duchemin, D. Jacquemin, and P.-F. Loos, The Bethe-Salpeter Equation Formalism: From Physics to Chemistry, *J. Phys. Chem. Lett.* **11**, 7371 (2020).
- [106] K. Merkel and F. Ortmann, Linear scaling approach for optical excitations using maximally localized Wannier functions, *J. Phys. Mater.* **7**, 015001 (2023).
- [107] M. Govoni and G. Galli, Large Scale GW Calculations, *J. Chem. Theory Comput.* **11**, 2680 (2015).
- [108] M. Kim, S. Mandal, E. Mikida, K. Chandrasekar, E. Bohm, N. Jain, Q. Li, R. Kanakagiri, G. J. Martyna, L. Kale, and S. Ismail-Beigi, Scalable GW software for quasiparticle properties using OpenAtom, *Comput. Phys. Commun.* **244**, 427 (2019).
- [109] D. Sangalli, A. Ferretti, H. Miranda, C. Attaccalite, I. Marri, E. Cannuccia, P. Melo, M. Marsili, F. Paleari, A. Marrazzo, G. Prandini, P. Bonfà, M. O. Atambo, F. Affinito, M. Palummo, A. Molina-Sánchez, C. Hogan, M. Grüning, D. Varsano, and A. Marini, Many-body perturbation theory calculations using the yambo code, *J. Phys. Condens. Matter* **31**, 325902 (2019).
- [110] M. Del Ben, H. Felipe, A. Canning, N. Wichmann, K. Raman, R. Sasanka, C. Yang, S. G. Louie, and J. Deslippe, Large-scale GW calculations on pre-exascale HPC systems, *Comput. Phys. Commun.* **235**, 187 (2019).
- [111] M. D. Ben, C. Yang, Z. Li, F. H. d. Jornada, S. G. Louie, and J. Deslippe, Accelerating Large-Scale Excited-State GW Calculations on Leadership HPC Systems, in *SC20: International Conference for High Performance Computing, Networking, Storage and Analysis* (2020) pp. 1–11.
- [112] V. W.-z. Yu and M. Govoni, GPU Acceleration of Large-Scale Full-Frequency GW Calculations, *J. Chem. Theory Comput.* **18**, 4690 (2022).
- [113] C.-N. Yeh, S. Isakov, D. Zgid, and E. Gull, Fully self-consistent finite-temperature GW in Gaussian Bloch orbitals for solids, *Phys. Rev. B* **106**, 235104 (2022).
- [114] I. Duchemin, D. Jacquemin, and X. Blase, Combining the gw formalism with the polarizable continuum model: A state-specific non-equilibrium approach, *J. Chem. Phys.* **144**, 164106 (2016).
- [115] J. Li, G. D’Avino, I. Duchemin, D. Beljonne, and X. Blase, Combining the Many-Body GW Formalism with Classical Polarizable Models: Insights on the Electronic Structure of Molecular Solids, *J. Phys. Chem. Lett.* **7**, 2814 (2016).
- [116] J. Li, G. D’Avino, I. Duchemin, D. Beljonne, and X. Blase, Accurate description of charged excitations in molecular solids from embedded many-body perturbation theory, *Phys. Rev. B* **97**, 035108 (2018).
- [117] J. Tölle, T. Deilmann, M. Rohlfing, and J. Neugebauer, Subsystem-Based GW/Bethe-Salpeter Equation, *J. Chem. Theory Comput.* **17**, 2186 (2021).
- [118] D. Amblard, X. Blase, and I. Duchemin, Many-body GW calculations with very large scale polarizable environments made affordable: A fully ab-initio QM/QM approach, *J. Chem. Phys.* **159**, 164107 (2023).
- [119] D. Amblard, X. Blase, and I. Duchemin, Static versus dynamically polarizable environments within the many-body GW formalism, *J. Chem. Phys.* **160**, 154104 (2024).
- [120] H. N. Rojas, R. W. Godby, and R. J. Needs, Space-Time Method for Ab Initio Calculations of Self-Energies and Dielectric Response Functions of Solids, *Phys. Rev. Lett.* **74**, 1827 (1995).
- [121] M. M. Rieger, L. Steinbeck, I. D. White, H. N. Rojas, and R. W. Godby, The GW space-time method for the self-energy of large systems, *Comput. Phys. Commun.* **117**, 211 (1999).
- [122] D. Foerster, P. Koval, and D. Sánchez-Portal, An $\mathcal{O}(N^3)$ implementation of Hedin’s GW approximation for molecules, *J. Chem. Phys.* **135**, 074105 (2011).
- [123] D. Neuhauser, Y. Gao, C. Arntsen, C. Karshenas, E. Rabani, and R. Baer, Breaking the Theoretical Scaling Limit for Predicting Quasiparticle Energies: The Stochastic GW Approach, *Phys. Rev. Lett.* **113**, 076402 (2014).
- [124] P. Liu, M. Kaltak, J. Klimeš, and G. Kresse, Cubic scaling GW: Towards fast quasiparticle calculations, *Phys. Rev. B* **94**, 165109 (2016).
- [125] V. Vlček, E. Rabani, D. Neuhauser, and R. Baer, Stochastic GW calculations for molecules, *J. Chem. Theory Comput.* **13**, 4997 (2017).
- [126] V. Vlček, W. Li, R. Baer, E. Rabani, and D. Neuhauser, Swift GW beyond 10,000 electrons using sparse stochastic compression, *Phys. Rev. B* **98**, 075107 (2018).
- [127] W. Gao and J. R. Chelikowsky, Accelerating Time-Dependent Density Functional Theory and GW Calculations for Molecules and Nanoclusters with Symmetry Adapted Interpolative Separable Density Fitting, *J. Chem. Theory Comput.* **16**, 2216 (2020).
- [128] J. Wilhelm, D. Golze, L. Talirz, J. Hutter, and C. A. Pignedoli, Toward GW Calculations on Thousands of Atoms, *J. Phys. Chem. Lett.* **9**, 306–312 (2018).
- [129] I. Duchemin and X. Blase, Separable resolution-of-the-identity with all-electron Gaussian bases: Application to cubic-scaling RPA, *J. Chem. Phys.* **150**, 174120 (2019).
- [130] A. Förster and L. Visscher, Low-Order Scaling G_0W_0 by Pair Atomic Density Fitting, *J. Chem. Theory Comput.* **16**, 7381–7399 (2020).
- [131] M. Kim, G. J. Martyna, and S. Ismail-Beigi, Complex-time shredded propagator method for large-scale GW calculations, *Phys. Rev. B* **101**, 035139 (2020).
- [132] A. L. Kutepov, Self-consistent GW method: $\mathcal{O}(N)$ algorithm for polarizability and self energy, *Comput. Phys. Commun.* **257**, 107502 (2020).
- [133] W. Gao, W. Xia, P. Zhang, J. R. Chelikowsky, and J. Zhao, Numerical methods for efficient GW calculations and the applications in low-dimensional systems, *Electron. Struct.* **4**, 023003 (2022).
- [134] J. Wilhelm, P. Seewald, and D. Golze, Low-Scaling GW with Benchmark Accuracy and Application to Phosphorene Nanosheets, *J. Chem. Theory Comput.* **17**, 1662 (2021).
- [135] C.-N. Yeh and M. A. Morales, Low-Scaling Algorithms for GW and Constrained Random Phase Approximation Using Symmetry-Adapted Interpolative Separable Density Fitting, *J. Chem. Theory Comput.* **20**, 3184 (2024).
- [136] R. Shi, P. Lin, M.-Y. Zhang, L. He, and X. Ren, Subquadratic-scaling real-space random phase approximation correlation energy calculations for periodic systems with numerical atomic orbitals, *Phys. Rev. B* **109**, 035103 (2024).
- [137] A. Förster and L. Visscher, Low-order scaling quasiparticle self-consistent GW for molecules, *Front. Chem.* **9**, 736591 (2021).
- [138] A. Förster and L. Visscher, Quasiparticle Self-Consistent GW-Bethe-Salpeter Equation Calculations for Large Chromophoric Systems, *J. Chem. Theory Comput.* **18**, 6779

- (2022).
- [139] E. Spadetto, P. H. T. Philipsen, A. Forster, and L. Visscher, Toward Pair Atomic Density Fitting for Correlation Energies with Benchmark Accuracy, *J. Chem. Theory Comput.* **19**, 1499 (2023).
 - [140] D. Golze, M. Iannuzzi, and J. Hutter, Local Fitting of the Kohn–Sham Density in a Gaussian and Plane Waves Scheme for Large-Scale Density Functional Theory Simulations, *J. Chem. Theory Comput.* **13**, 2202 (2017).
 - [141] J. Lu and L. Ying, Compression of the electron repulsion integral tensor in tensor hypercontraction format with cubic scaling cost, *J. Comput. Phys.* **302**, 329 (2015).
 - [142] J. Lu and K. Thicke, Cubic scaling algorithms for RPA correlation using interpolative separable density fitting, *J. Comput. Phys.* **351**, 187 (2017).
 - [143] I. Duchemin and X. Blase, Cubic-Scaling All-Electron GW Calculations with a Separable Density-Fitting Space–Time Approach, *J. Chem. Theory Comput.* **17**, 2383 (2021).
 - [144] F. A. Delesma, M. Leucke, D. Golze, and P. Rinke, Benchmarking the accuracy of the separable resolution of the identity approach for correlated methods in the numeric atom-centered orbitals framework, *J. Chem. Phys.* **160**, 024118 (2024).
 - [145] W. Gao, Z. Tang, J. Zhao, and J. R. Chelikowsky, Efficient Full-Frequency GW Calculations Using a Lanczos Method, *Phys. Rev. Lett.* **132**, 126402 (2024).
 - [146] O. Vahtras, J. Almlöf, and M. Feyereisen, Integral approximations for LCAO-SCF calculations, *Chem. Phys. Lett.* **213**, 514 (1993).
 - [147] Y. Jung, A. Sodt, P. M. Gill, and M. Head-Gordon, Auxiliary basis expansions for large-scale electronic structure calculations, *Proc. Natl. Acad. Sci. U.S.A.* **102**, 6692 (2005).
 - [148] M. Azizi, J. Wilhelm, D. Golze, M. Giantomassi, R. L. Panadés-Barrueta, F. A. Delesma, A. Bucchieri, A. Gulans, P. Rinke, C. Draxl, and X. Gonze, Time-frequency component of the GreenX library: minimax grids for efficient RPA and GW calculations, *J. Open Source Softw.* **8**, 5570 (2023).
 - [149] M. Azizi, J. Wilhelm, D. Golze, F. A. Delesma, R. L. Panadés-Barrueta, P. Rinke, M. Giantomassi, and X. Gonze, Validation of the GreenX library time-frequency component for efficient GW and RPA calculations, *Phys. Rev. B* **109**, 245101 (2024).
 - [150] J. Tölle, N. Niemeyer, and J. Neugebauer, Accelerating Analytic-Continuation GW Calculations with a Laplace Transform and Natural Auxiliary Functions, *J. Chem. Theory Comput.* **20**, 2022 (2024).
 - [151] J. P. Perdew, K. Burke, and M. Ernzerhof, Generalized Gradient Approximation Made Simple, *Phys. Rev. Lett.* **77**, 3865 (1996).
 - [152] W. Kohn and L. J. Sham, Self-Consistent Equations Including Exchange and Correlation Effects, *Phys. Rev.* **140**, A1133 (1965).
 - [153] F. Caruso, M. Dauth, M. J. van Setten, and P. Rinke, Benchmark of GW Approaches for the GW100 Test Set, *J. Chem. Theory Comput.* **12**, 5076–5087 (2016).
 - [154] S. J. Bintrim and T. C. Berkelbach, Full-frequency GW without frequency, *J. Chem. Phys.* **154**, 041101 (2021).
 - [155] C. J. C. Scott, O. J. Backhouse, and G. H. Booth, A “moment-conserving” reformulation of GW theory, *J. Chem. Phys.* **158**, 124102 (2023).
 - [156] E. Monino and P.-F. Loos, Connections and performances of Green’s function methods for charged and neutral excitations, *J. Chem. Phys.* **159**, 034105 (2023).
 - [157] I. Duchemin and X. Blase, Robust Analytic-Continuation Approach to Many-Body GW Calculations, *J. Chem. Theory Comput.* **16**, 1742 (2020).
 - [158] W. Gao and J. R. Chelikowsky, Real-Space Based Benchmark of G_0W_0 Calculations on GW100: Effects of Semicore Orbitals and Orbital Reordering, *J. Chem. Theory Comput.* **15**, 5299 (2019).
 - [159] M. J. van Setten, F. Weigend, and F. Evers, The GW-method for quantum chemistry applications: Theory and implementation, *J. Chem. Theory Comput.* **9**, 232 (2013).
 - [160] C. A. Ullrich, *Time-Dependent Density-Functional Theory: Concepts and Applications* (Oxford University Press, 2011).
 - [161] G. Onida, L. Reining, and A. Rubio, Electronic excitations: density-functional versus many-body Green’s-function approaches, *Rev. Mod. Phys.* **74**, 601 (2002).
 - [162] A. Marie, A. Ammar, and P.-F. Loos, *The GW Approximation: A Quantum Chemistry Perspective* (2024), arXiv:2311.05351.
 - [163] Q. Sun, X. Zhang, S. Banerjee, P. Bao, M. Barbry, N. S. Blunt, N. A. Bogdanov, G. H. Booth, J. Chen, Z.-H. Cui, J. J. Eriksen, Y. Gao, S. Guo, J. Hermann, M. R. Hermes, K. Koh, P. Koval, S. Lehtola, Z. Li, J. Liu, N. Mardirossian, J. D. McClain, M. Motta, B. Mussard, H. Q. Pham, A. Pulkin, W. Purwanto, P. J. Robinson, E. Ronca, E. R. Sayfutyarova, M. Scheurer, H. F. Schurkus, J. E. T. Smith, C. Sun, S.-N. Sun, S. Upadhyay, L. K. Wagner, X. Wang, A. White, J. D. Whitfield, M. J. Williamson, S. Wouters, J. Yang, J. M. Yu, T. Zhu, T. C. Berkelbach, S. Sharma, A. Y. Sokolov, and G. K.-L. Chan, Recent developments in the PySCF program package, *J. Chem. Phys.* **153**, 024109 (2020).
 - [164] M. Véril, P. Romaniello, J. A. Berger, and P.-F. Loos, Unphysical Discontinuities in GW Methods, *J. Chem. Theory Comput.* **14**, 5220 (2018).
 - [165] K. Siegbahn, C. Nordling, G. Johansson, J. Hedman, P. F. Hedén, K. Hamrin, U. Gelius, T. Bergmark, L. O. Werme, R. Manne, and Y. Baer, *ESCA applied to free molecules* (North-Holland Publishing Company Amsterdam-London, 1969) pp. 51–136.
 - [166] J. Schirmer, G. Angonoa, S. Svensson, D. Nordfors, and U. Gelius, High-energy photoelectron c 1s and o 1s shake-up spectra of CO, *J. Phys. B: At. Mol. Opt. Phys.* **20**, 6031 (1987).
 - [167] M. L. M. Rocco, M. Haeming, D. R. Batchelor, R. Fink, A. Schöll, and E. Umbach, Electronic relaxation effects in condensed polyacenes: A high-resolution photoemission study, *J. Chem. Phys.* **129**, 074702 (2008).
 - [168] T. J. Pollehn, A. Schindlmayr, and R. W. Godby, Assessment of the GW approximation using Hubbard chains, *J. Phys. Condens. Matter* **10**, 1273 (1998).
 - [169] M. Gatti, G. Panaccione, and L. Reining, Effects of Low-Energy Excitations on Spectral Properties at Higher Binding Energy: The Metal-Insulator Transition of VO₂, *Phys. Rev. Lett.* **114**, 116402 (2015).
 - [170] J. S. Zhou, J. J. Kas, L. Sponza, I. Reshetnyak, M. Guzzo, C. Giorgetti, M. Gatti, F. Sottile, J. J. Rehr, and L. Reining, Dynamical effects in electron spectroscopy, *J. Chem. Phys.* **143**, 184109 (2015).
 - [171] R. M. Martin, L. Reining, and D. M. Ceperley, *Interacting Electrons: Theory and Computational Approaches* (Cambridge University Press, 2016).
 - [172] J. D. Lee, O. Gunnarsson, and L. Hedin, Transition from the adiabatic to the sudden limit in core-level photoemission, *Phys. Rev. B* **60**, 8034 (1999).
 - [173] H. J. Vidberg and J. W. Serene, Solving the Eliashberg equations by means of N-point Padé approximants, *J. Low Temp. Phys.* **29**, 179 (1977).
 - [174] L. V. Ahlfors, *Complex analysis*, Vol. 3 (McGraw-Hill New York, 1979), uniqueness theorem is discussed on p. 127.

- [175] S. L. Adler, Quantum theory of the dielectric constant in real solids, *Phys. Rev.* **126**, 413 (1962).
- [176] N. Wiser, Dielectric constant with local field effects included, *Phys. Rev.* **129**, 62 (1963).
- [177] R. W. Godby, M. Schlüter, and L. J. Sham, Self-energy operators and exchange-correlation potentials in semiconductors, *Phys. Rev. B* **37**, 10159 (1988).
- [178] S. Lebègue, M. Klintonberg, O. Eriksson, and M. I. Katsnelson, Accurate electronic band gap of pure and functionalized graphane from GW calculations, *Phys. Rev. B* **79**, 245117 (2009).
- [179] X. Gonze, B. Amadon, P.-M. Anglade, J.-M. Beuken, F. Bottin, P. Boulanger, F. Bruneval, D. Caliste, R. Caracas, M. Côté, T. Deutsch, L. Genovese, P. Ghosez, M. Giantomassi, S. Goedecker, D. Hamann, P. Hermet, F. Jollet, G. Jomard, S. Leroux, M. Mancini, S. Mazevet, M. Oliveira, G. Onida, Y. Pouillon, T. Rangel, G.-M. Rignanese, D. Sangalli, R. Shaltaf, M. Torrent, M. Verstraete, G. Zerah, and J. Zwanziger, ABINIT: First-principles approach to material and nanosystem properties, *Comput. Phys. Commun.* **180**, 2582 (2009).
- [180] T. D. Kühne, M. Iannuzzi, M. Del Ben, V. V. Rybkin, P. Seewald, F. Stein, T. Laino, R. Z. Khaliullin, O. Schütt, F. Schiffmann, D. Golze, J. Wilhelm, S. Chulkov, M. H. Bani-Hashemian, V. Weber, U. Borštnik, M. Tailliefumier, A. S. Jakobovits, A. Lazzaro, H. Pabst, T. Müller, R. Schade, M. Guidon, S. Andermatt, N. Holmberg, G. K. Schenter, A. Hehn, A. Bussy, F. Belleflamme, G. Tabacchi, A. Glöb, M. Lass, I. Bethune, C. J. Mundy, C. Plessl, M. Watkins, J. VandeVondele, M. Krack, and J. Hutter, CP2K: An electronic structure and molecular dynamics software package - Quickstep: Efficient and accurate electronic structure calculations, *J. Chem. Phys.* **152**, 194103 (2020).
- [181] CP2K, <https://www.cp2k.org>, <https://github.com/cp2k/cp2k> (accessed 15 March 2024).
- [182] G. Lippert, J. Hutter, and M. Parrinello, The Gaussian and augmented-plane-wave density functional method for ab initio molecular dynamics simulations, *Theor. Chem. Acc.* **103**, 124 (1999).
- [183] F. Weigend, F. Furche, and R. Ahlrichs, Gaussian basis sets of quadruple zeta valence quality for atoms H–Kr, *J. Chem. Phys.* **119**, 12753 (2003).
- [184] C. Hättig, Optimization of auxiliary basis sets for RI-MP2 and RI-CC2 calculations: Core–valence and quintuple-zeta basis sets for H to Ar and QZVPP basis sets for Li to Kr, *Phys. Chem. Chem. Phys.* **7**, 59 (2005).
- [185] M. Kaltak, J. Klimes, and G. Kresse, Low Scaling Algorithms for the Random Phase Approximation: Imaginary Time and Laplace Transformations, *J. Chem. Theory Comput.* **10**, 2498 (2014).
- [186] D. Golze, N. Benedikter, M. Iannuzzi, J. Wilhelm, and J. Hutter, Fast evaluation of solid harmonic Gaussian integrals for local resolution-of-the-identity methods and range-separated hybrid functionals, *J. Chem. Phys.* **146**, 034105 (2017).
- [187] E. F. Valeev, Libint, A library for the evaluation of molecular integrals of operators over Gaussian functions, <https://github.com/evaleev/libint> (accessed 15 March 2024).
- [188] V. Blum, R. Gehrke, F. Hanke, P. Havu, V. Havu, X. Ren, K. Reuter, and M. Scheffler, Ab initio molecular simulations with numeric atom-centered orbitals, *Comput. Phys. Commun.* **180**, 2175 (2009).
- [189] X. Ren, P. Rinke, V. Blum, J. Wieferink, A. Tkatchenko, A. Sanfilippo, K. Reuter, and M. Scheffler, Resolution-of-identity approach to Hartree–Fock, hybrid density functionals, RPA, MP2 and GW with numeric atom-centered orbital basis functions, *New J. Phys.* **14**, 053020 (2012).
- [190] A. Takatsuka, S. Ten-no, and W. Hackbusch, Minimax approximation for the decomposition of energy denominators in Laplace-transformed Møller–Plesset perturbation theories, *J. Chem. Phys.* **129**, 044112 (2008).
- [191] M. Del Ben, O. Schütt, T. Wentz, P. Messmer, J. Hutter, and J. VandeVondele, Enabling simulation at the fifth rung of DFT: Large scale RPA calculations with excellent time to solution, *Comput. Phys. Commun.* **187**, 120 (2015).
- [192] B. Helmich-Paris and L. Visscher, Improvements on the minimax algorithm for the Laplace transformation of orbital energy denominators, *J. Comput. Phys.* **321**, 927 (2016).
- [193] W. Hackbusch, Computation of best L^∞ exponential sums for $1/x$ by Remez’ algorithm, *Comput. Vis. Sci.* **20**, 1 (2019).
- [194] M. Häser and J. Almlöf, Laplace transform techniques in Møller–Plesset perturbation theory, *J. Chem. Phys.* **96**, 489 (1992).
- [195] P. Y. Ayala and G. E. Scuseria, Linear scaling second-order Møller–Plesset theory in the atomic orbital basis for large molecular systems, *J. Chem. Phys.* **110**, 3660 (1999).
- [196] D. S. Lambrecht, B. Doser, and C. Ochsenfeld, Rigorous integral screening for electron correlation methods, *J. Chem. Phys.* **123**, 184102 (2005).
- [197] D. Kats, D. Usvyat, and M. Schütz, On the use of the Laplace transform in local correlation methods, *Phys. Chem. Chem. Phys.* **10**, 3430 (2008).
- [198] D. Kats, D. Usvyat, S. Loibl, T. Merz, and M. Schütz, Comment on “Minimax approximation for the decomposition of energy denominators in Laplace-transformed Møller–Plesset perturbation theories” [*J. Chem. Phys.* **129**, 044112 (2008)], *J. Chem. Phys.* **130**, 127101 (2009).
- [199] GreenX, <https://github.com/nomad-coe/greenX> (accessed 15 March 2024).
- [200] K. Krause, M. E. Harding, and W. Klopper, Coupled-cluster reference values for the GW27 and GW100 test sets for the assessment of GW methods, *Mol. Phys.* **113**, 1952 (2015).
- [201] D. Bellert, K. L. Burns, R. Wampler, and W. Breckenridge, An accurate determination of the ionization energy of the MgO molecule, *Chem. Phys. Lett.* **322**, 41 (2000).
- [202] J. Heyd, G. E. Scuseria, and M. Ernzerhof, Hybrid functionals based on a screened Coulomb potential, *J. Chem. Phys.* **118**, 8207 (2003).
- [203] In case of issues with HSE06 orbitals, one might consider quasiparticle-selfconsistent GW (qsGW) [210].
- [204] Y. Yao, D. Golze, P. Rinke, V. Blum, and Y. Kanai, All-Electron BSE@GW Method for K-Edge Core Electron Excitation Energies, *J. Chem. Theory Comput.* **18**, 1569 (2022).
- [205] F. Fuchs, J. Furthmüller, F. Bechstedt, M. Shishkin, and G. Kresse, Quasiparticle band structure based on a generalized Kohn–Sham scheme, *Phys. Rev. B* **76**, 115109 (2007).
- [206] M. Schambeck, NOMAD repository GW calculations on O₃, BeO, MgO, BN, CuCN (2024).
- [207] M. Schambeck, https://github.com/miasb/GW_calculations_03_BeO_MgO_BN_CuCN (accessed 28 May 2024).
- [208] M. E. Casida, Time-dependent density functional response theory for molecules, in *Recent Advances in Density Functional Methods*, pp. 155–192.
- [209] C. Adamo and V. Barone, Toward reliable density functional methods without adjustable parameters: The PBE0 model, *J. Chem. Phys.* **110**, 6158 (1999).
- [210] M. van Schilfgaarde, T. Kotani, and S. Faleev, Quasiparticle Self-Consistent GW, *Phys. Rev. Lett.* **96**, 226402 (2006).